Medium modifications for light and heavy nuclear clusters in simulations of core collapse supernovae: Impact on equation of state and weak interactions

Tobias Fischer,[1,*] Stefan Typel,[2,3] Gerd Röpke,[4] Niels-Uwe F. Bastian,[1] and Gabriel Martínez-Pinedo[3,2,5]

[1]*Institute for Theoretical Physics, University of Wrocław, plac Maksa Borna 9, 50-204 Wrocław, Poland*

[2]*Technische Universität Darmstadt, Fachbereich Physik, Institut für Kernphysik, Schlossgartenstraße 9, 64289 Darmstadt, Germany*

[3]*GSI Helmholtzzentrum für Schwerionenforschung, Theorie, Planckstraße 1, 64291 Darmstadt, Germany*

[4]*Institut für Physik, Universität Rostock, Albert-Einstein-Straße 23 - 24, 18059 Rostock, Germany*

[5]*Helmholtz Forschungsakademie Hessen für FAIR, GSI Helmholtzzentrum für Schwerionenforschung, Planckstraße 1, 64291 Darmstadt, Germany*

(Received 26 August 2020; revised 28 October 2020; accepted 9 November 2020; published 25 November 2020)

The present article investigates the role of heavy nuclear clusters and weakly bound light nuclear clusters based on a newly developed equation of state for core collapse supernova studies. A novel approach is brought forward for the description of nuclear clusters, taking into account the quasiparticle approach and continuum correlations. It demonstrates that the commonly employed nuclear statistical equilibrium approach, based on noninteracting particles, for the description of light and heavy clusters becomes invalid for warm nuclear matter near the saturation density. This has important consequences for studies of core collapse supernovae. To this end, we implement this nuclear equation of state provided for arbitrary temperature, baryon density, and isospin asymmetry, to spherically symmetric core collapse supernova simulations to study the impact on the dynamics as well as on the neutrino emission. For the inclusion of a set of weak processes involving light clusters the rate expressions are derived, including medium modifications at the mean-field level. A substantial impact from the inclusion of a variety of weak reactions involving light clusters on the post bounce dynamics and on the neutrino emission could not be found.

DOI: 10.1103/PhysRevC.102.055807

I. INTRODUCTION

A core collapse supernova (SN) is associated with the gravitational collapse of a massive star's core at the end of its life, due to the loss of the dominant pressure from the degenerate electron gas. This is caused by electron captures on protons bound in nuclei and is accompanied by the photodisintegration of heavy nuclei. A protoneutron star (PNS) forms at the center when the density exceeds nuclear saturation density during the stellar core contraction. Then, the short-range repulsive nuclear interaction in homogeneous nuclear matter halts the collapse, a hydrodynamics shock wave forms and the core bounces back. This instant is defined when the maximum central density is reached, corresponding to the moment just before the shock breakout. The shock wave stalls during its initial propagation out of the core due to the dissociation of still infalling heavy nuclei and the deleptonization associated with ν_e-losses when the shock wave propagates across the neutrinosphere. The revival of the stalled bounce shock, i.e., the SN problem, is related to the liberation of energy from the central PNS into the low-density layer behind the shock (for a review, cf. Ref. [1]). The shock revival to increasingly larger radii defines the onset of the SN explosion.

The SN conditions are wide spread, see Fig. 1(a) in Ref. [2], featuring temperatures of $T \simeq 0 - 100$ MeV, rest-mass densities of $\rho = 10^0 - 10^{15}$ g cm^{-3} and isospin asymmetry given by the charge density, or equivalent the proton abundance Y_p ranging from $Y_p = 0$ (neutron matter) to $Y_p = 1$ (proton matter). Note that the proton fraction equals the electron fraction, $Y_p = Y_e$, in the absence of other leptonic charges. For recent comprehensive reviews about core collapse SN phenomenology, see Refs. [3,4], discussing also the role of the equation of state (EOS) in SN simulations at the various different regimes encountered [2].

The EOS at the suprasaturation density, $\rho_0 = 2.5 \times 10^{14}$ g cm^{-3} (equivalent the nucleon number density, $n_0 = 0.15$ fm^{-3}), as well as high temperatures is often obtained from nuclear energy density functionals. These are often derived in a mean-field approximation for the interacting nucleons. At subsaturation densities and temperatures below few tens of MeV, inhomogeneous matter can be found where nuclear clusters as well as unbound nucleons are present in addition to pasta phases [5]. Even neglecting pasta phases, the description of the nuclear medium is particularly challenging. The commonly employed approaches for SN EOS are the single-nucleus approximation based on the liquid-drop model (see, e.g., Refs. [6,7] and references therein), the Thomas-Fermi approach of Ref. [8] and the modified nuclear statistical equilibrium (NSE) of Ref. [9] (see also Ref. [10]). Only the latter allows for the detailed nuclear composition to be taken

*tobias.fischer@uwr.edu.pl

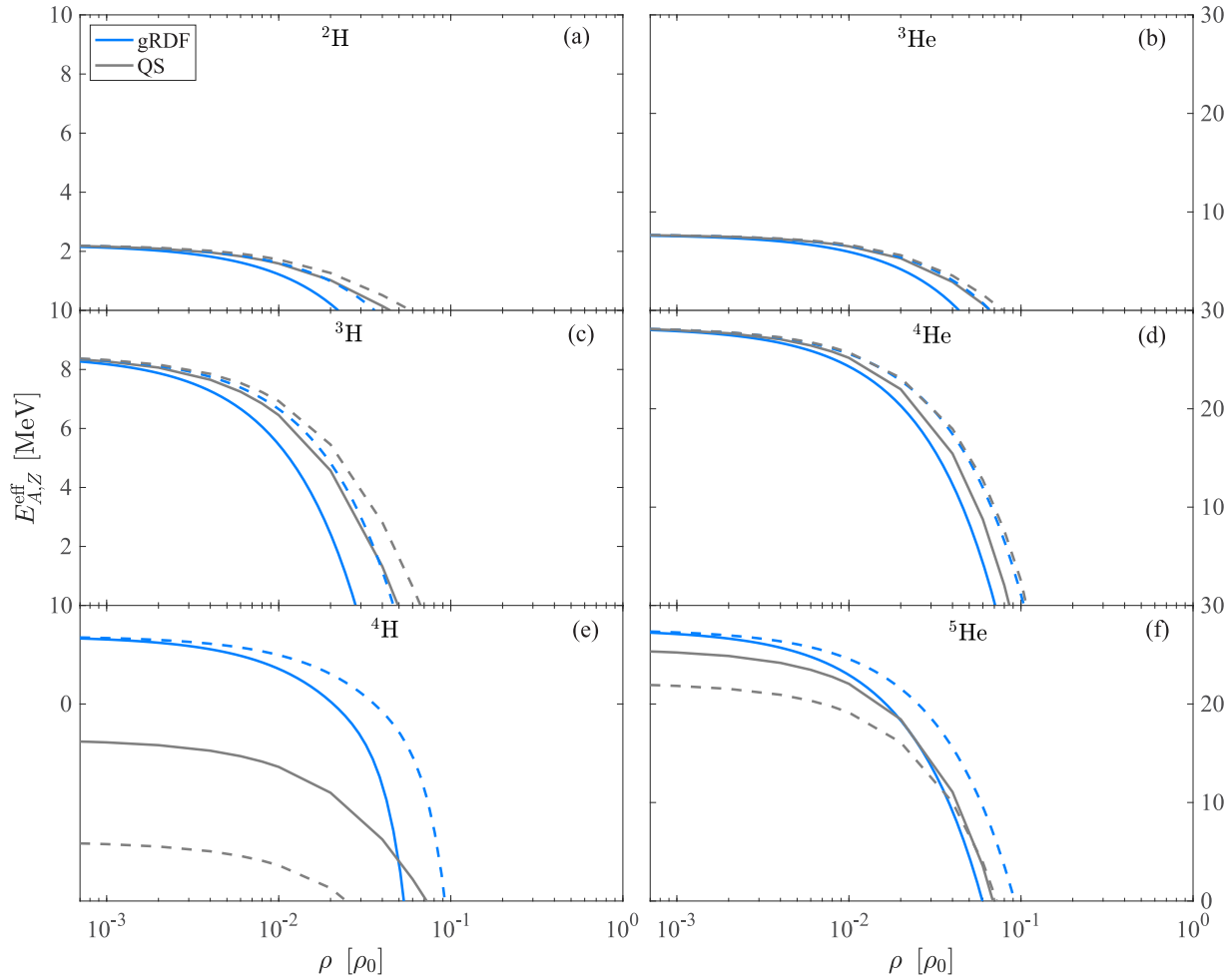

FIG. 1. Effective nuclear binding energy for selected hydrogen isotopes in graphs (a), (c), and (e), and helium isotopes in graphs (b), (d), and (f), for two representative conditions, with $T = 5$ MeV and $Y_e = 0.1$ (solid lines) as well as $T = 10$ MeV and $Y_e = 0.2$ (dashed lines), comparing the gRDF approach including a shift due to Pauli blocking (blue lines) and the QS approach of Ref. [17] (gray lines).

into account explicitly. It is based on several thousand nuclear species with tabulated (and partly calculated) nuclear masses, as well as a theoretical framework handling excited states which must be included at finite temperatures. In particular, about the role of light nuclear clusters, such as deuteron ^{2}H, has long been speculated [11]. The potential role of additional clusters, such as triton, ^{3}H, and helium-3, ^{3}He, has been pointed out in Ref. [12] as well as recently in Ref. [2], also its particular impact on the neutrino response [13]. Recently, even more *exotic* neutron rich isotopes have been studied in the context of core collapse SNe in Ref. [14] based on the simplistic NSE model of Ref. [9], which is based on nuclei treated as noninteracting Boltzmann particles.

Despite the success of this NSE approach, there are a number of caveats. Whereas the NSE is well suited to describe nuclear matter at low densities and high temperatures, the account of medium effects is necessary when going to higher densities ($\gtrsim 10^{12}$ g cm^{-3}). One of the most important issues is the transition to homogeneous matter when approaching the saturation density. The need to take density effects (medium modifications of the cluster properties) into account was demonstrated by laboratory experiments [15,16]. A quantum-statistical approach (see Ref. [17] and references given therein), has been worked out which describes a generalized virial expansion to account for correlations in the continuum. Self-energy and Pauli-blocking contributions are obtained from an in-medium few-nucleon Schrödinger equation. In the low-density region, the relation to the concept of excluded volume has been demonstrated in Ref. [18], and a generalized relativistic density-functional (gRDF) approach [19] which considers the light elements as new quasiparticles coupled to the mesonic fields. The semi-empirical approaches, i.e., excluded volume and gRDF, proved to be successful in describing laboratory experiments in the density region up to one fifth of the saturation density. A modification of the relativistic mean-field approach considering in-medium effects via an effective cluster-meson coupling has been proposed [20,21], where light clusters $A \leqslant 12$ have been taken into account.

It was demonstrated in Sec. 4 of Ref. [2], when comparing the modified NSE abundances (taking the excluded volume into account) for the light nuclear clusters and unbound nucleons with those obtained within the quantum statistical (QS) model of Refs. [22] and [23], that the NSE model of Ref. [9]

significantly overestimates the abundances of all light clusters in the density region $\rho \geqslant 10^{12}$ g cm^{-3}. Also the properties of the unbound nucleons are affected substantially. To quantify this impact in simulations of core collapse SNe, the present work expands the previous analysis, by means of developing a novel fully temperature and isospin asymmetry dependent SN EOS based on the gRDF model of Ref. [24], including self-consistently the description of light nuclear clusters (defined as nuclei with charge $Z \leqslant 2$) and heavy clusters ($Z > 2$) as well as the transition to homogeneous matter. The gRDF approach implements medium modified nuclear binding energies (see Ref. [17]) that are derived to match the QS approach, as well as continuum correlations described by the virial expansion, which ensures the appropriate transition to homogeneous matter. This has important consequences for the SN dynamics and neutrino emission. To study systematically the differences obtained in comparison to the NSE EOS of Ref. [9], henceforth denoted as HS, we implement the gRDF EOS into the SN model AGILE-BOLTZTRAN and simulate the post bounce evolution in spherical symmetry. We implement the same density dependent mean-field parametrization (denoted as DD2) of Ref. [19], for both EOS henceforth denoted as gRDF(DD2) and HS(DD2) (The HS EOS catalog is provided by CompOSE [25] and has been subject to extensive comparison studies, cf., Ref. [26] and references therein).

Neutrinos emitted from a core collapse SN contain a broad spectrum of information, e.g., they probe the EOS deep inside the SN core which is otherwise hidden. The future neutrino detection from the next galactic event will shed light not only on details of the yet controversially discussed explosion mechanism, it may also reveal properties of matter at conditions which are currently inaccessible in nuclear physics experiments. It is of paramount interest to predict reliable neutrino luminosities and spectra, as well as their evolution, for such events. Of particular importance is the role of the hot and dense nuclear medium. Besides weak processes involving the unbound nucleons, the role of heavy nuclear clusters has long been studied, i.e., for nuclear electron capture rates [27] as well as neutrino-nucleus scattering (see Ref. [28] and references therein) and nuclear (de)excitations [29,30]. The previous implementation of weak charged current reactions with light nuclear clusters in core collapse SN simulations has so far still been approximate [11]. The gRDF(DD2) EOS, subject to the present paper, contains the detailed composition, including all light clusters. This allows us to extend the previous attempts and include a variety of weak processes, involving the hydrogen isotopes with atomic mass numbers $A = 2$–7 and the helium isotopes with $A = 3$–7, into the simulations of the SN post bounce evolution. In particular, we discuss the significance of exotic, neutron-rich H (e.g., ^{4}H) and He (e.g., ^{5}He) isotopes near the saturation density as proposed recently by Ref. [14] within the simple NSE model of Ref. [9]. This approach overestimates the abundances of these light clusters as shown recently in Ref. [17] within the QS formalism. The account of the light element isotopes leads to a reduction of the neutrino luminosities and an enhancement of the spectral differences between ν_e and $\bar{\nu}_e$. However, a substantial impact from the inclusion of a variety of weak reactions involving light clusters could not be found, neither on the post bounce dynamics nor on the neutrino emission.

TABLE I. Standard set of weak reactions considered in this work, including references.

	Weak process	Reference
1	$e^- + p \rightleftarrows n + \nu_e$	[31]
2	$e^+ + n \rightleftarrows p + \bar{\nu}_e$	[31]
3	$n \rightleftarrows p + e^- + \bar{\nu}_e$	[31]
4	$e^- + (A, Z) \rightleftarrows (A, Z-1) + \nu_e$	[32]
5	$\nu + N \rightleftarrows \nu' + N$	[33,34][a]
6	$\nu + (A, Z) \rightleftarrows \nu' + (A, Z)$	[33][a]
7	$\nu + e^\pm \rightleftarrows \nu' + e^\pm$	[35][a]
8	$e^- + e^+ \rightleftarrows \nu + \bar{\nu}$	[36][a]
9	$N + N \rightleftarrows \nu + \bar{\nu} + N + N$	[37,38][a]
10	$\nu_e + \bar{\nu}_e \rightleftarrows \nu_{\mu/\tau} + \bar{\nu}_{\mu/\tau}$	[39,40]
11	$\nu + \bar{\nu} + (A, Z) \rightleftarrows (A, Z)^*$	[29,30][a]

[a] $\nu = \{\nu_e, \bar{\nu}_e, \nu_{\mu/\tau}, \bar{\nu}_{\mu/\tau}\}$ and $N = \{n, p\}$.

The manuscript is organized as follows. In Sec. II the SN model is briefly reviewed. The newly developed gRDF(DD2) EOS is introduced in Sec. III, in comparison to the modified NSE EOS, while in Sec. IV simulations of core collapse SN are discussed, comparing the reference simulation with gRDF(DD2) EOS and the NSE approach. The analysis is extended in Sec. V introducing weak reactions with light clusters and performing additional SN simulations. The manuscript closes with the summary in Sec. VI.

II. SUPERNOVA MODEL

The SN model employed in this study, AGILE-BOLTZTRAN, is based on general relativistic neutrino-radiation hydrodynamics in spherical symmetry with three-flavor Boltzmann neutrino transport [33,41,42]. It features a Lagrangian mass mesh with an adaptive mesh refinement method, originally developed in Ref. [43] and updated in Ref. [40]. The complete set of standard weak reactions considered in this work can be found in Table I, including the references. Here we use a neutrino discretization in terms of 36 energy bins of $E_\nu \in [0.5, 300]$ MeV and 6 momentum scattering angles, $\mu = \cos\theta \in \{-1, +1\}$, for the neutrino flavors $\{\nu_e, \bar{\nu}_e, \nu_{\mu/\tau}, \bar{\nu}_{\mu/\tau}\}$. The implicit method solving the Boltzmann equation on an adaptive Lagrangian mass mesh has been compared with other commonly employed neutrino-transport schemes, e.g., the multigroup flux limited diffusion approximation [42], the variable Eddington factor technique [44] and with M1 schemes [45], resulting in good qualitative agreement. AGILE-BOLTZTRAN has a flexible EOS-module that can handle many currently available baryon EOS [6,9,46–48]. For conditions that correspond to the non-NSE regime at low temperatures, precisely below $T = 0.45$ MeV, we switch to a baryon EOS based on the ideal gas of silicon and sulfur nuclei. It is meant to resemble the remaining silicon–sulphur layer of the progenitor star. In addition to the baryons, contributions from $e^\pm$, photons and Coulomb are added [49].

Particular focus has been devoted to the consistent description of the charged current processes, reactions (1)–(3)

in Table I, and the nuclear EOS (for details, see Ref. [50]), with the implementation of the nucleon mean-field potentials, U_n and U_p [51,52]. The latter are related to the scalar Σ_N^S, Eq. (A9), and vector parts Σ_N^V, Eq. (A7), of the nucleon self energies (see Appendix A for further details), $U_N = \Sigma_N^V - \Sigma_N^S$ (see also Ref. [53] and references therein). In particular, their difference, $U_n - U_p$, is determined by the nuclear symmetry energy which has a strong density dependence [54].

Of special importance for the SN dynamics, including neutrino heating and cooling, are the weak processes involving the unbound nucleons. The largest inverse mean-free paths are found for the neutral current neutrino nucleon scattering processes, reaction (5) in Table I, and the largest energy transfer contributions originate from the charged current absorption and emission reactions (1)–(3) in Table I. Therefore, not only the consistent description of the weak reaction rates and EOS, including their implementation into the transport module, are of importance but also the properties of the unbound nucleons, which in turn are determined by the nuclear EOS as well. In particular, the nucleon self-energies, which are related to the nucleon effective masses and the mean-field potentials, have a direct impact on the weak rates for both, neutral- and charged current processes (for details, see also Ref. [31] and references therein). More precisely, at conditions of low degeneracy, all these reaction rates are proportional to the number density of the target nucleons. Hence it is important to implement the correct description of the nucleon properties which are strongly affected by the presence of nuclear clusters in the inhomogeneous nuclear matter phase. This will be further discussed and illustrated in the following section.

III. EQUATION OF STATE WITH LIGHT AND HEAVY CLUSTERS

A theoretical model for the EOS used in simulations of core collapse SNe has to provide both the thermodynamic properties and the chemical composition of matter in a wide range of densities, temperatures, and isospin asymmetries. In the present application, the gRDF approach is employed which includes nucleons, nuclei, electrons, muons, and photons as degrees of freedom. The energy density functional was derived in the mean-field approximation from a relativistic Lagrangian density. It describes the effective in-medium interaction between nucleons (free and bound in clusters) by an exchange of ω, σ and ρ mesons with density dependent couplings using the DD2 parametrization [19]. The latter was fitted to properties of finite nuclei. The set of nuclei in the density functional comprises light ($Z \leqslant 2$) and heavy nuclei ($Z > 2$) with experimental binding energies of the Atomic Mass Evaluation 2016 [55]. This table was supplemented with more exotic nuclei of unknown experimental binding energy using the DZ31 model of Ref. [56] for their masses. Excited states of heavy nuclei are included effectively with temperature-dependent degeneracy factors (details can be found in Ref. [24]). The effects of the nuclear medium on the properties of nuclear clusters is modelled in the gRDF approach by implementing nuclear mass shifts that lead to effective binding energies different from their vacuum value. In addition to previous gRDF models that considered only ^{2}H, ^{3}H, ^{3}He, and ^{4}He as light nuclei, the present calculation incorporates additional neutron-rich isotopes. These include the following hydrogen isotopes ^{4}H, ^{5}H, ^{6}H, and ^{7}H, as well as the following helium isotopes ^{5}He, ^{6}He, and ^{7}He. All these exotic nuclei have a positive nuclear binding energy in vacuum [55], but some of them have a negative neutron separation energy are hence unstable with respect to neutron emission, or β decay as in the case of ^{6}He. Thus they can be described as resonances in the continuum.

To implement these additional light clusters, including their medium modifications, into the equation of state, the QS approach is employed (cf. Ref. [57]). The latter is based on a many-particle theory which defines Green's functions and spectral densities. Thermodynamic relations are derived consistently. A few-body, in-medium Schrödinger equation can be given which describes bound states as well as scattering states of the A-nucleon cluster, where the influence of the nuclear medium is described by self-energy and Pauli blocking terms. As a consequence, the bound state energies and wave functions as well as the scattering phase shifts of the A-nucleon cluster become dependent on the properties of the medium, i.e., the temperature T, the density ρ, and the charge density. This way, the quasiparticle concept which is well-known for the single-nucleon states is generalized to nuclear cluster states like the α particle. In Appendix B the formulas are given for the virial expansion and generalized Beth-Uhlenbeck equation, for the example of the deuteron system with a single bound state and a continuum of scattering states. Similarly, ^{4}H and ^{5}He systems can be treated this way. In these cases, no bound states exist, and only the integral over the scattering states remains in Eq. (B1) in Appendix B. The chemical potentials contain the the information about the density of neutrons and protons. An effective cluster energy $E_{A,Z}^{\rm eff}$, cf., Eq. (B2), can be introduced which depends strongly on the temperature but also on the density. Details are discussed in Ref. [17] where analytical expressions for the T and ρ dependence of $E_{A,Z}^{\rm eff}$ for ^{4}H and ^{5}He are given.

The dissolution of nuclei with increasing temperature and density is described in the gRDF model with the help of medium-dependent mass shifts that include a small contribution from the screened Coulomb interaction and the strong-interaction shifts originating from Pauli blocking, as introduced above. The concept of mass shifts replaces the excluded-volume approach that was used in the modified NSE EOS of Ref. [9]. At present, while the QS approach can be applied to only a few selected light nuclear species, gRDF allows for the universal description of in-medium properties. Individual calculations of the energy shifts and continuum correlations for each isotope $\{A, Z\}$, in particular for heavy clusters with large mass numbers A are presently not available. Therefore an approximate treatment applicable for arbitrary nuclei is necessary, as given by the gRDF approach. The functional form of the Pauli shift denoted as model GRDF2 in Ref. [58] was used for heavy nuclei and the functional form of the Pauli mass shifts of the nuclei ^{4}H, ^{5}H, and ^{5}He was assumed to be identical to one of the closest stable nucleus in the same isotopic chain. Details on the theoretical formulation of the gRDF are given in Appendix A. Further details on the parametrization of the gRDF(DD2) can be found in

Refs. [24,58,59]. The effective nuclear binding energies are shown in Fig. 1, for selected clusters with $Z = 1$ (left panel) and $Z = 2$ (right panel). Here we compare the gRDF EOS (blue lines) with the QS calculations (gray lines) of Ref. [17]. For the bound nuclei ^{2}H, ^{3}H, ^{3}He, ^{4}He, the effective binding energies approach the corresponding ground-state binding energy values at low densities. A weak temperature dependence is seen in the QS approach because of the account of scattering states leading to the virial form of the EOS. This effect of continuum correlations becomes small at low temperatures when states above the continuum edge are not excited. A strong temperature dependence, illustrated at two examples, $T = 5$ MeV and $T = 10$ MeV, is seen for the unbound nuclei ^{4}H and ^{5}He which appear as a broad resonance above the edge of the ^{3}H–n and ^{4}He–n continuum so that the contribution to the EOS is given only by the scattering phase shifts. As a consequence, the temperature effects are strong, as known from the virial expansion. However, for lower temperatures on the order of $T = 1$ MeV the continuum contributions become less dominant and the effective in-medium nuclear binding energy for ^{4}H and ^{5}He rises toward the vacuum binding energy value, and hence gRDF and QS agree with each other at these conditions. Furthermore, for the important transition toward the regime where the light cluster dissolve, both gRDF and QS provide good qualitative agreement, with the slightly earlier drop of $E^{\rm eff}_{A,Z}$ for all light clusters within gRDF (see Fig. 1) resulting in the dissolving of light clusters at slightly lower density (see Figs. 2 and 3), compared to the QS framework.

None of these aspects are captured within the NSE framework where vacuum binding energies are employed and the scattering state contributions are ignored. Consequently, the abundances of bound states are generally overestimated within the NSE approach so that it fails to describe the disappearance of bound states near the saturation density and the transition to homogeneous nuclear matter (Mott effect). This transition is a consequence of in-medium effects (Pauli blocking) and is modeled by the excluded volume approach as well as the generalized relativistic density-functional approach.

Figures 2 and 3 show the nuclear composition of selected species at same conditions as in Fig. 1 ($T = 5$ MeV, $Y_e = 0.1$ and $T = 10$ MeV, $Y_e = 0.2$) with respect to the density in units of the saturation density, comparing the modified NSE EOS (thin black lines) of Ref. [9] henceforth denoted as HS(DD2) and the gRDF(DD2) EOS of this work (thick blue lines). Plotted is the density range relevant for the SN evolution; very low densities where in-medium effects are not relevant, are omitted here. With increasing density when nuclear clusters become abundant, the deviations between both approaches grow substantially. There arise four major differences:

(1) The HS(DD2) EOS systematically overestimates the abundances of light clusters. In particular in the region where gRDF(DD2) predicts already the complete dissolution of all light clusters, HS(DD2) still finds substantial abundances. This caveat is related to the description of nuclear clusters in general within HS(DD2), where the geometric excluded volume approach is employed for the dissolution of clusters. It cannot distinguish between heavy and light clusters and does not include a temperature dependence. However, gRDF(DD2) is based on in-medium modified binding energies for heavy and light nuclear clusters. Consequently, the yields of all hydrogen and helium

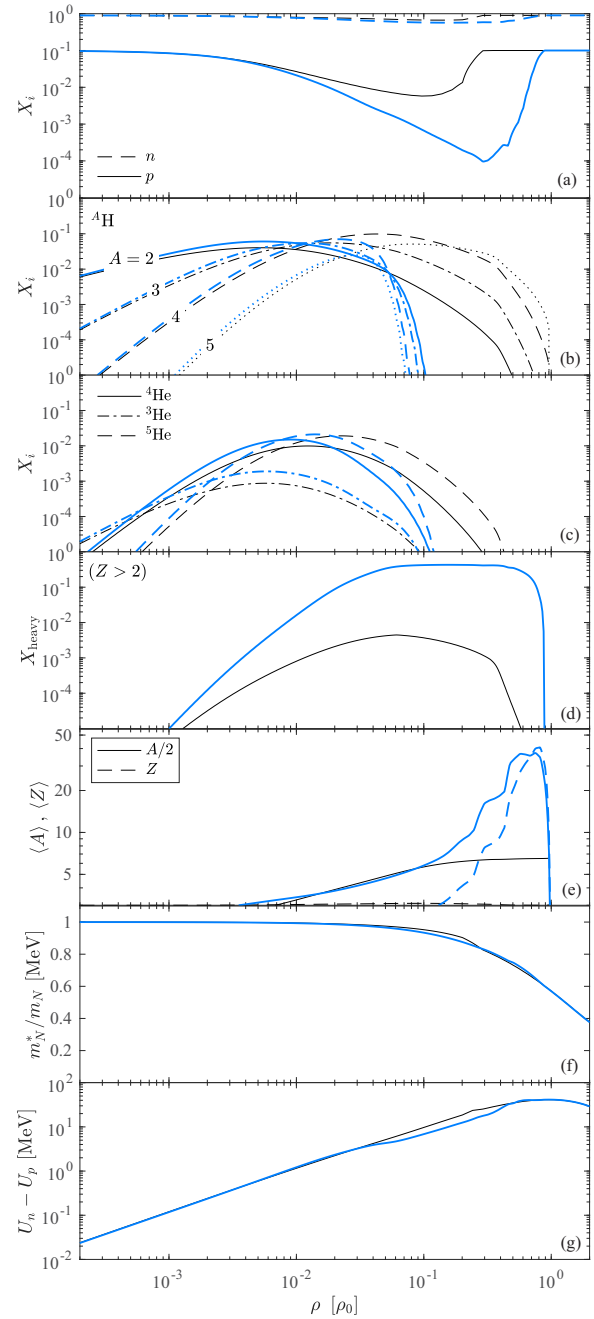

FIG. 2. Nuclear composition; mass fractions for neutrons and protons in graph (a), hydrogen isotopes in graph (b), helium isotopes in graph (c), and for heavy nuclei averaging over all species with $Z > 2$ in graph (d), as well as their average atomic mass A and charge Z in graph (e), and furthermore including the nucleon effective mass m_N^* in graph (f), and the mean-field potential difference $U_n - U_p$ in graph (g), as a function of the restmass density ρ in units of the saturation density ρ_0, comparing the HS(DD2) modified NSE model (black lines) of Ref. [9] and the gRDF(DD2) model (blue lines) for selected condition, $T = 5$ MeV and $Y_e = 0.1$.

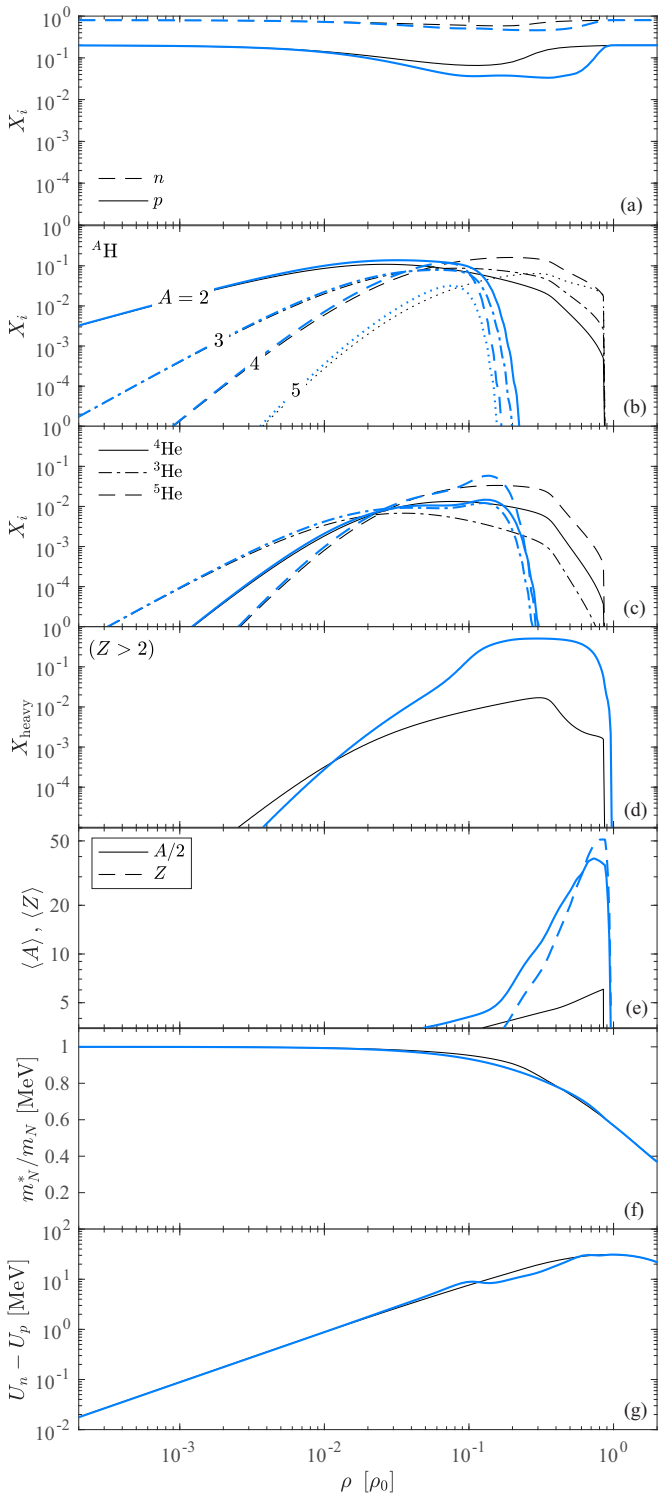

FIG. 3. The same quantities are shown in graphs (a)–(g) as in Fig. 2 but for different conditions, $T = 10$ MeV and $Y_e = 0.2$.

clusters drop to zero at lower density, as illustrated in Figs. 2 and 3, in agreement with their effective nuclear binding energies dropping below zero (see Fig. 1).

(2) Of interest is that the abundances of exotic, neutron-rich isotopes such as the hydrogen isotopes ^{4}H, ^{5}H, ^{6}H but also the helium isotopes ^{5}He, ^{6}He, ^{7}He, ^{8}He, are strongly reduced within the gRDF(DD2) approach at densities above one tenth of the saturation density, in comparison with HS(DD2). This strong reduction of the gRDF framework is in contrast to Ref. [14] where plots similar to Figs. 2 and 3 are given, considering only the excluded volume concept of the HS(DD2) model. This suppression is further enhanced in the QS approach if accounting for continuum correlation as given by scattering phase shifts. The Beth-Uhlenbeck formula is an exact expression for the second virial coefficient and may serve as a benchmark for any EOS in the low-density limit [60–64]. Generalizations considering higher clusters and the introduction of the quasiparticle picture need special attention to be consistent and to avoid double counting. Calculations have been performed for the exotic nuclei ^{4}H, ^{5}He (see Ref. [17]). The QS approach including continuum correlations is not available at present for arbitrary nuclei so that we focus on the gRDF(DD2) approach which provides us with an appropriate description of in-medium effects for arbitrary bound nuclei.

(3) The in-medium nuclear binding energies for the heavy clusters ($Z > 2$) of gRDF(DD2) results in substantial abundances at higher density, than for the NSE approach HS(DD2). Also the average nuclear charge and mass numbers, $\langle Z \rangle$ and $\langle A \rangle$, respectively, are substantially different. In particular, the heavy nuclei within gRDF(DD2) are less neutron rich than for HS(DD2), partly related to their shift toward higher density.

(4) Note the systematically lower abundance of ^{4}He at low densities for the gRDF(DD2) EOS in comparison with HS(DD2), which is a attributed to the Coulomb shift of the heavy clusters due to electron screening effects. Note that the latter are not included in the HS EOS. In fact, the Coulomb shifts are larger than the Pauli shifts at these low densities (and low temperatures). It results in an enhancement of the in-medium nuclear binding energy for the heavy clusters. Consequently, there are simultaneously more heavy cluster and less ^{4}He at these conditions. This effect becomes even more pronounced at less isospin asymmetric conditions, which will become relevant when discussing the SN simulation results below.

The different description of the light and heavy nuclear clusters feeds back to the abundances of the unbound nucleons (see the top panel in Figs. 2 and 3). Largest differences between HS(DD2) and gRDF(DD2) are found in the density domain corresponding to the dissolution of the light clusters at intermediate densities between $\rho = 0.05 - 0.5 \times \rho_0$ and the presence of heavy clusters at higher density. It results in a substantially lower abundance of neutrons and protons at these densities. Consequently also the nucleon self energies are modified at the same densities (see the two bottom panels in Figs. 2 and 3). All this has already been studied in great detail in Ref. [24]. It has important consequences for the SN evolution, which will be illustrated and discussed in the next section.

We give some arguments why we think that the gRDF(DD2) EOS is more appropriate than the HS(DD2) EOS. The gRDF(DD2) EOS is closely related to the QS approach and is consistent with all presently known constraints. It matches the neutron matter calculations of chiral perturbation theory at subsaturation density (see Refs. [65,66] and references therein) and pulsar observations. The latter refer to a neutron star radius of about 13 km for a neutron star mass of 1.4 $M_\odot$, in agreement with the constraint obtained from the gravitational wave analysis of the inspiral phase of the first binary neutron star merger events GW170817 and GW190425 [67–69], being in agreement with the first NICER data analysis [70], as well as a maximum neutron star mass of 2.42 $M_\odot$ in agreement with the high-precision observations of the presently most massive pulsars [71,72].

IV. gRDF EOS IN CORE COLLAPSE SN SIMULATIONS

The core collapse SN simulations which will be discussed in the following are launched from the 18 $M_\odot$ progenitor provided by the stellar evolution series of Ref. [73]. This progenitor series has already been subject to a variety of SN EOS studies, e.g., within the failed SN branch and the subsequent black hole formation [40], exploring the role of the nuclear symmetry energy [54] and the role of the stiffness/softness of the supersaturation density phase [74]. Here, we compare the reference simulation with the HS(DD2) EOS, which has been the foundation for our previous studies, and the newly developed and implemented gRDF(DD2) EOS. The standard set of weak processes is included (see Table I). SN simulations with weak processes involving light clusters will be discussed further below.

A. Stellar core collapse and bounce

The stellar core collapse evolution is governed by the presence of heavy nuclear clusters at low densities and temperatures below $T = 1$ MeV. Nuclear electron captures (reaction (4) in Table I) and nuclear de-excitation processes (reaction (11) in Table I) give rise to neutrino losses. Since the heavy cluster component of HS(DD2) and gRDF(DD2) match at these conditions, the entire collapse phases proceeds identical. Only shortly before core bounce, when central densities close to nuclear saturation density and temperatures in excess of several MeV are reached, differences between HS(DD2) and gRDF(DD2) arise. This is illustrated in Fig. 4 at about 0.1 ms before core bounce. While nearly all heavy clusters are already dissolved for HS(DD2), they are still substantially abundant for the simulation with gRDF(DD2).

The presence of a large abundance of heavy clusters at high density softens the EOS in that density domain, which has important consequences for the SN bounce dynamics. Density and temperature are notably lower for gRDF(DD2), compared to HS(DD2), in the region where heavy clusters are still abundant (see Fig. 4). The central density at core bounce, shown in Fig. 5, is substantially lower for gRDF(DD2), $\rho_{\rm central} = 2.72 \times 10^{14}$ g cm^{-3}, in comparison to HS(DD2), $\rho_{\rm central} = 3.32 \times 10^{14}$ g cm^{-3}. The energy gain due to compression work is converted into nuclear binding energy of the heavy clusters. This prevents the central density from quickly

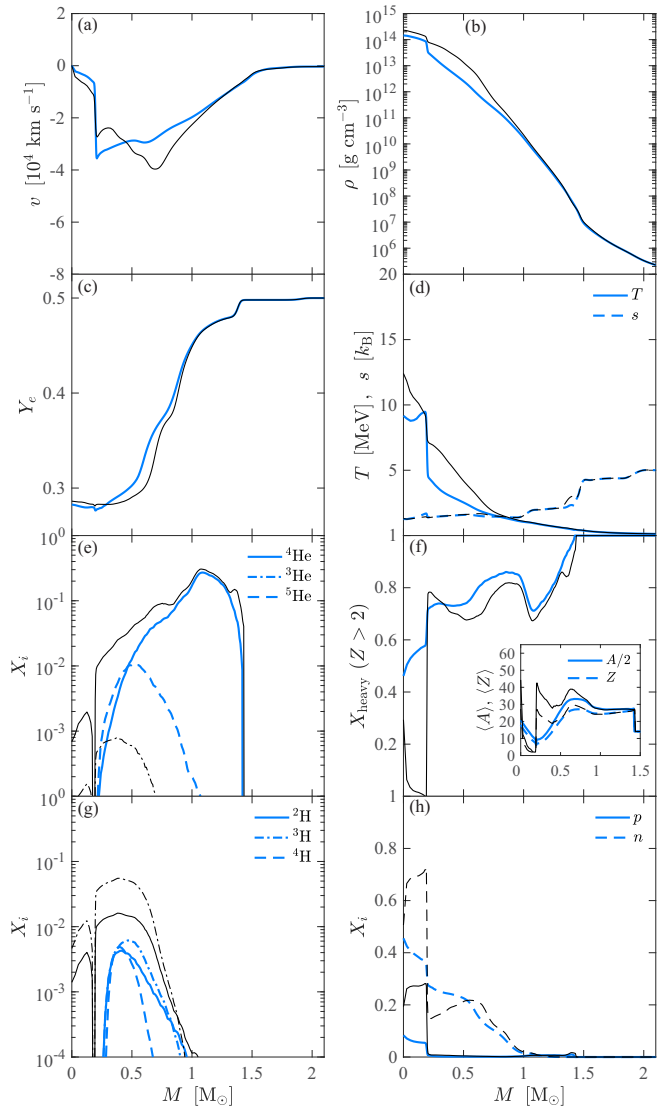

FIG. 4. Radial profiles of selected quantities; velocity u in graph (a), restmass density ρ in graph (b), electron fraction Y_e in graph (c), temperature T and entropy per baryon s in graph (d), as well as various mass fraction X_i in graphs (e), (g), and (h), and the heavy nuclei in graph (f) as well as the composition characterised by the average atomic mass $\langle A \rangle$ and charge $\langle Z \rangle$, as a function of the enclosed baryon mass M at about 0.5 ms before core bounce, comparing two SN simulations with the HS(DD2) EOS of Ref. [9] (black lines) and the newly developed gRDF(DD2) EOS (blue lines).

rising above the saturation density for the simulation with gRDF(DD2). A large subsaturation density domain remains where heavy clusters still exist for gRDF(DD2) (see Fig. 5), featuring also lower temperatures than HS(DD2). However, the electron fraction Y_e is affected only marginally. During the final core collapse phase the Y_e differences can be attributed to the different nuclear composition of the heavy clusters. Already before core bounce, when the condition of weak equilibrium is obtained and the neutrino trapping regime has formed, corresponding to the high-temperature region of the collapsing stellar core where $T \gtrsim 5$ MeV, the slight differences of the central Y_e obtained are due to the different

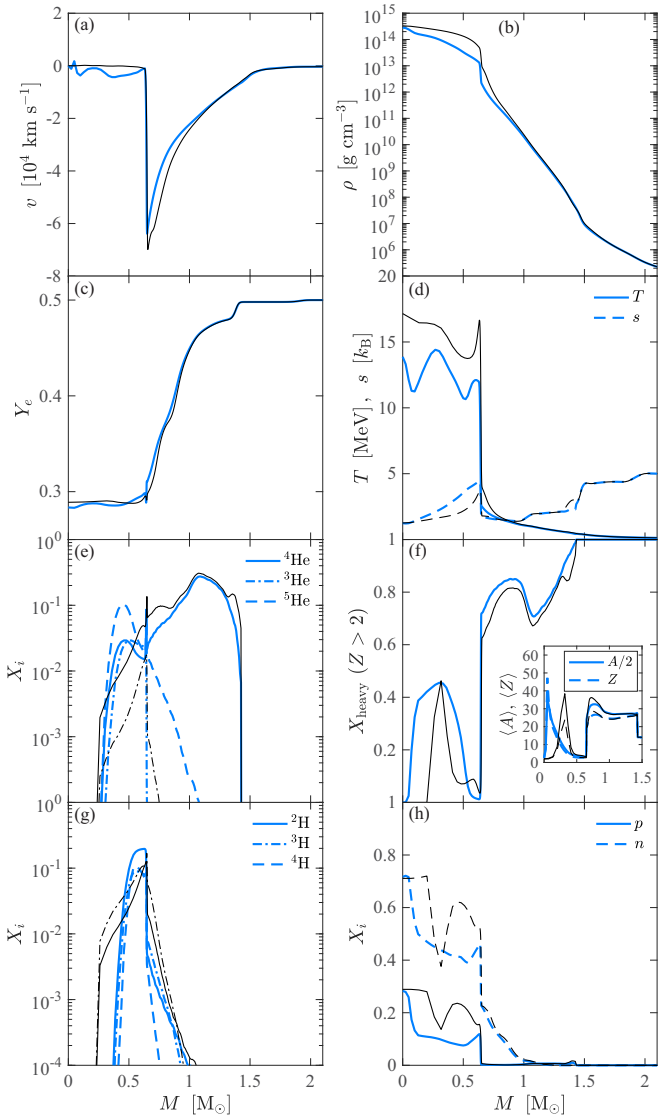

FIG. 5. The same quantities are shown in graphs (a)–(h) as in Fig. 4 but at core bounce.

density and temperature profiles, where lower density and temperature for gRDF(DD2) feature lower Y_e illustrated in Fig. 5 at core bounce.

As expected from Ref. [24] and the analysis in Sec. III, the abundances of all light clusters are substantially overestimated for HS(DD2) in the region where they already disappear within gRDF(DD2) toward high density. This aspect is particularly important for the newly introduced neutron rich hydrogen and helium isotopes, e.g., ^{4}H and ^{5}He. In the following we will focus only on these two isotopes since heavier hydrogen and helium isotopes are less abundant at the conditions of relevance here (see Figs. 2 and 3) and play hence a minor role for the SN dynamics and neutrino emission. Already during the final core collapse phase, shown in Fig. 4, all light clusters are abundant. This has already been discussed in Refs. [11,47,75] and recently in Ref. [14], however, the latter two without performing SN simulations with light clusters explicitly taken into account. Moreover, the larger abundance of all light clusters of the statistical model of HS(DD2), in comparison to gRDF(DD2), is a feedback from having lower densities with the latter SN simulations due to the presence of heavy clusters in this density domain. Only toward higher densities, the geometric excluded volume approach of HS(DD2) overestimates the abundances of all light clusters, in comparison where gRDF(DD2) already predicts their complete dissolution. Note further that HS(DD2) does not contain any other helium nuclei besides ^{3}He and ^{4}He, which results in the significantly overestimated abundance of ^{3}He. This is particularly important since at the neutron rich conditions encountered at the stellar core collapse, featuring $Y_e \simeq 0.25$–0.3, the proton rich nucleus ^{3}He should be strongly suppressed. This is the case for gRDF(DD2) treating in addition ^{5}He which, in fact, becomes more abundant then ^{4}He under neutron rich conditions toward high density (see Fig. 4).

B. Post bounce evolution

During the early post-bounce evolution, the situation remains the same as before core bounce and the differences reported previously between HS(DD2) and gRDF(DD2) still hold, as illustrated in Figs. 6 and 7 at two selected post bounce times. Only when the temperature starts to exceed $T \simeq 15$ MeV the heavy nuclear clusters of gRDF(DD2) dissolve, transition into the state of homogeneous nuclear matter at around 100 ms post bounce and the SN evolution using HS(DD2) and gRDF(DD2) become increasingly similar (see therefore Fig. 7 showing radial profiles of selected quantities at 100 ms post bounce). However, the higher temperatures obtained for the gRDF(DD2) EOS reflect the systematically softer EOS during the later SN post bounce evolution, beyond 100 ms. This has two important consequences, higher temperatures enable (1) higher abundances of light clusters, as illustrated at 300 ms post bounce in Fig. 8, and (2) a more compact PNS which in turn results in a smaller shock radius already before shock stalling (see the top panel in Fig. 9). In particular, the faster shock retreat results in a faster PNS compression, which in turn supports even higher temperatures at the PNS interior (see Fig. 8).

It it important to note further the presence of ^{5}He—a nuclear cluster which has not been considered before in simulations of core collapse SNe—in the neutron rich PNS interior. The abundance of ^{5}He exceeds even the abundance of ^{4}He by more than one order of magnitude, due to the generally neutron-rich conditions featuring $Y_e \simeq 0.1$–0.25, as illustrated in the sequences shown in the Figs. 7 and 8. Similarly, ^{4}H is found to be as abundant as ^{3}H in the region of their highest population. This is partly supported due to the neutron-rich conditions, given by the electron fraction of $Y_e \simeq 0.1 - 0.2$ (see Fig. 8). The presence of a large amount of light clusters at high densities, in the range of $\rho = 10^{12}$–10^{14} g cm^{-3}, softens the nuclear EOS in this regime substantially, which in turn results in systematically higher temperatures (see Figs. 6–8).

Note further the systematically higher abundance of heavy clusters and lower abundance of ^{4}He in the post-shock layer and ahead of the SN accretion shock, corresponding to low densities $\rho < 10^{10}$ g cm^{-3} as well as low temperatures $T < 2.5$ MeV and nearly isospin symmetric conditions with

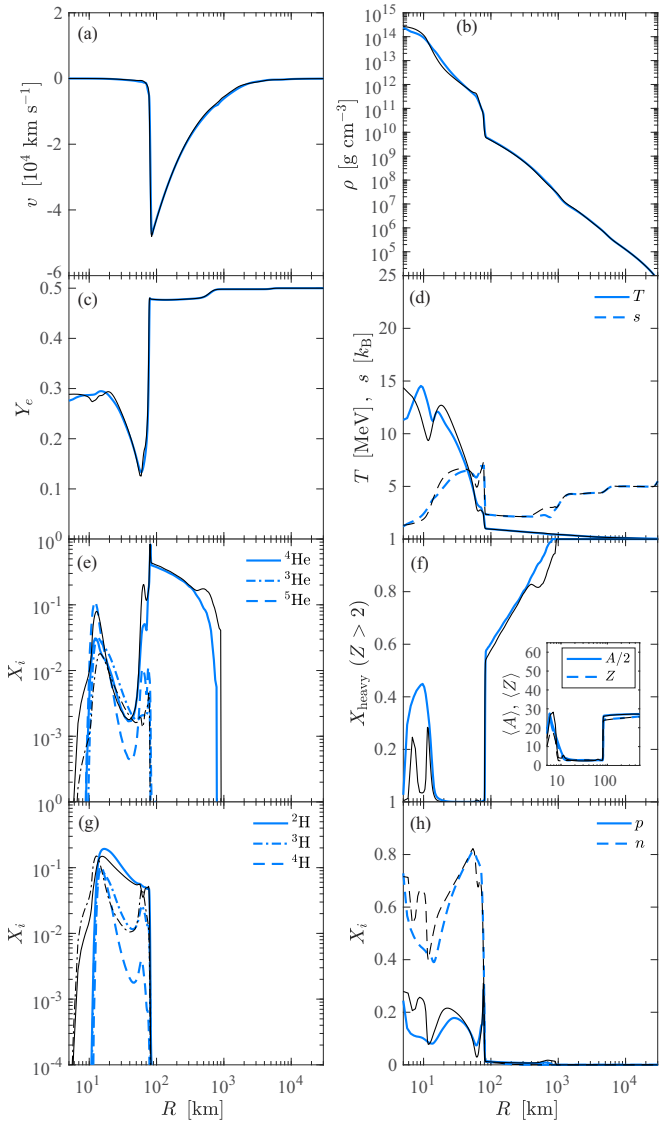

FIG. 6. The same quantities are shown in graphs (a)–(h) as in Fig. 4 but with respect to the radius R at 10 ms after core bounce.

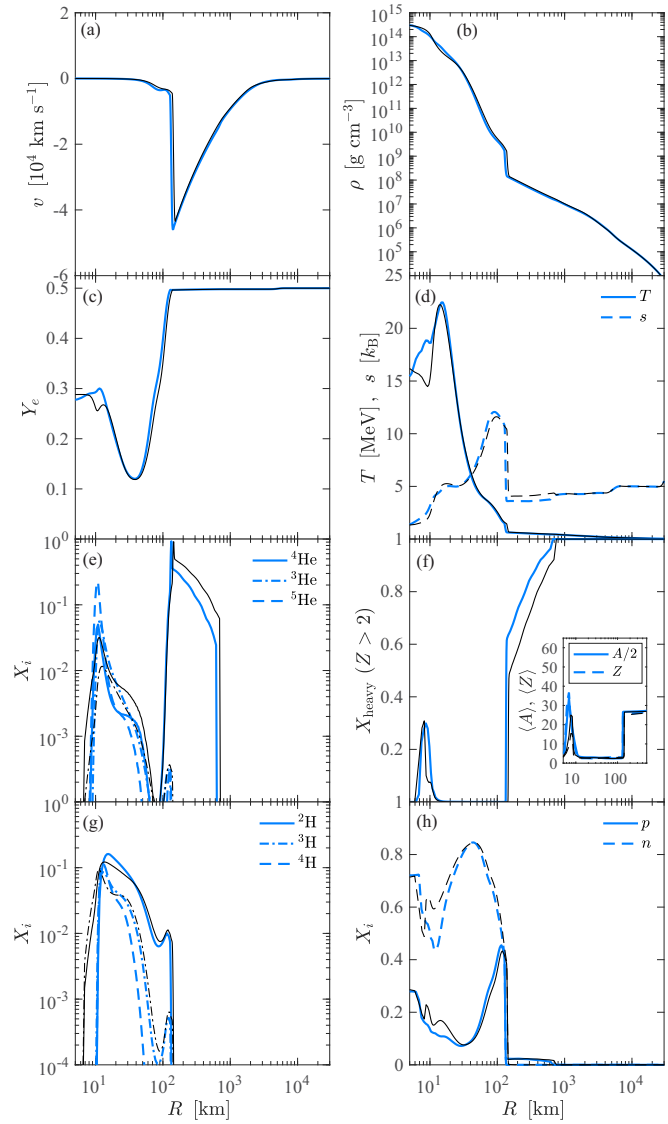

FIG. 7. The same quantities are shown in graphs (a)–(h) as in Fig. 4 but with respect to the radius R at 100 ms after core bounce.

$Y_e \simeq 0.45$–0.5 (see Figs. 5–8). This is the region where the Coulomb shifts enhance the nuclear binding energy of the heavy clusters, as discussed above in Sec. III.

C. Neutrino emission

The softer gRDF(DD2) EOS and the associated faster shock retreat result in an increase of the luminosities of all neutrino flavors during the early post bounce evolution up to about 100 ms, as illustrated in Fig. 10. The impact is largest for $\bar{\nu}_e$ and the heavy-lepton flavor neutrinos, which decouple at highest densities where the impact from the more compact PNS is largest, compared to the ν_e. However, during the later post bounce phase $\gtrsim$200–250 ms, the luminosities of gRDF(DD2) match those obtained for the simulation using HS(DD2).

The three bottom panels of Fig. 9 show the evolution of the ν_e, $\bar{\nu}_e$, and $\nu_{\mu/\tau}$ neutrinosphere radii, as well as the corresponding densities denoted as ρ_ν in the inlays. The steeper density gradient at the PNS surface obtained for the SN simulation with the softer gRDF(DD2) EOS, results in a shift of all neutrinospheres toward smaller radii already after about 50–75 ms post bounce. This is a direct feedback from the softer gRDF(DD2) EOS and the subsequent faster PNS contraction. Complementary, the density at the neutrinospheres is shifted to slightly higher values, comparing HS(DD2) and gRDF(DD2), as shown in the inlays of Fig. 9, featuring a slightly higher temperature. The latter aspect gives rise to generally higher average neutrino energies for all flavors for the SN simulation based on the softer gRDF(DD2) EOS, as illustrated in the bottom panels of Fig. 10. The largest increase of the average energies is obtained also for ν_e and $\bar{\nu}_e$, which decouple at lowest density in the layer of accumulated material at the PNS surface where the impact from the more compact PNS is largest for the gRDF(DD2) EOS, than for

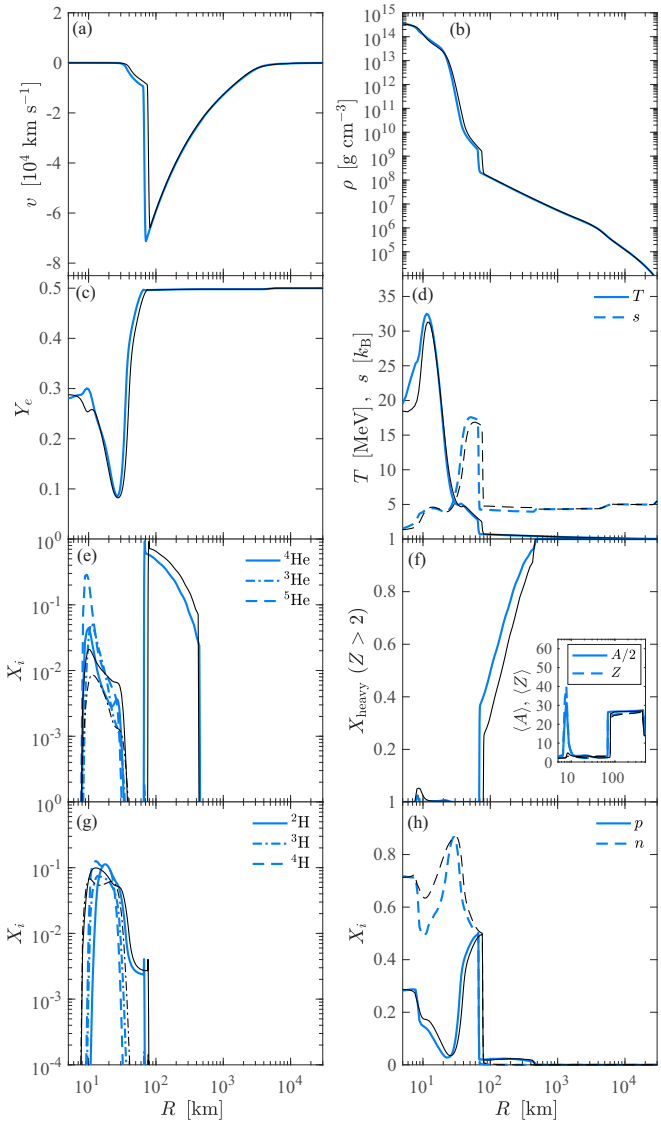

FIG. 8. The same quantities are shown in graphs (a)–(h) as in Fig. 4 but with respect to the radius R at 300 ms after core bounce.

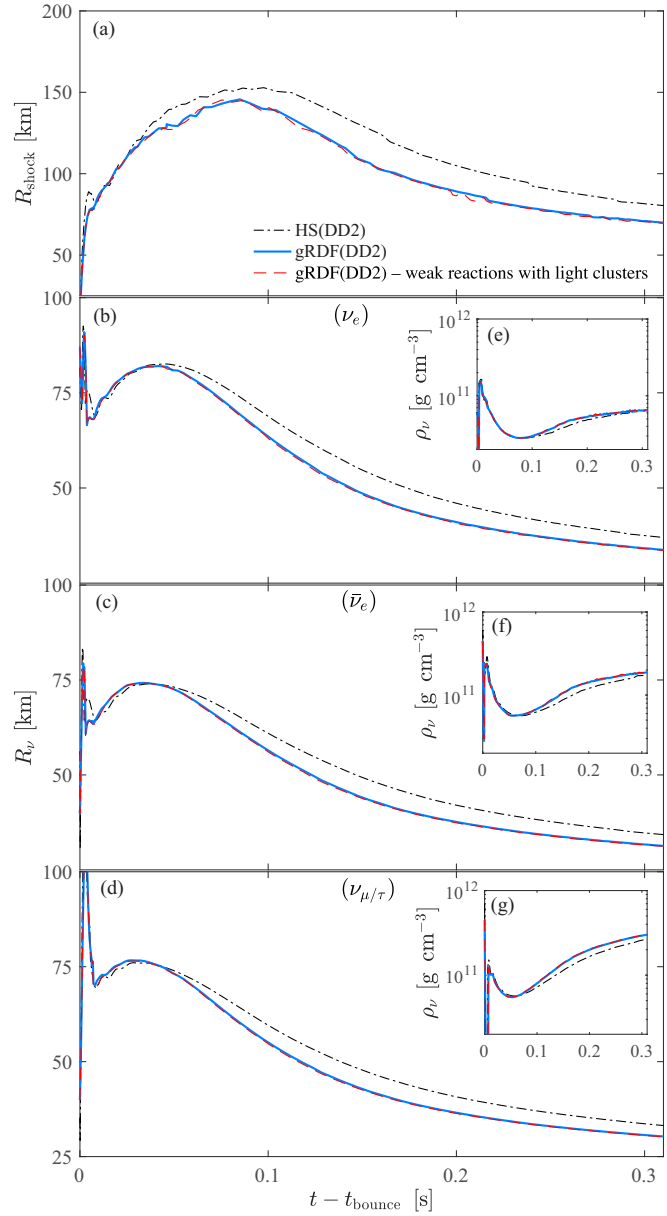

FIG. 9. Post bounce evolution of the shock radii, $R_{\rm shock}$, in graphs (a) and of the neutrinospheres, R_ν, for ν_e in graph (b) and $\bar{\nu}_e$ in graph (c) as well as muon- and tau-(anti)neutrinos collectively denoted as $\nu_{\mu/\tau}$ in graph (d) and the corresponding densities, ρ_ν, for ν_e in graph (e) and $\bar{\nu}_e$ in graph (f) as well as muon- and tau-(anti)neutrinos $\nu_{\mu/\tau}$ in graph (g), comparing the SN simulations based on the HS(DD2) EOS (black lines) and the generalized relativistic density-functional approach gDRF(DD2) without (blue lines) and with weak processes involving light clusters (red lines). Note that the latter two lay indistinguishably on top of each other (see text for details).

the heavy lepton neutrino flavors denoted as $\nu_{\mu/\tau}$ and $\bar{\nu}_{\mu/\tau}$ in Figs. 9 and 10.

These generally higher neutrino fluxes and average energies during the long-term post bounce evolution are well known features for SN simulations employing soft EOS. However, here we are able to relate the softness of gRDF(DD2) to the presence of a large fraction of light isospin asymmetric nuclear clusters which are either neglected previously or taken incorrectly into account based on the NSE approach.

V. ROLE OF WEAK REACTIONS WITH LIGHT CLUSTERS

Then presence of light nuclear clusters enables a variety of weak processes. The ones considered here are listed in Table II. These concern the charged current neutrino emission and absorption of ν_e and $\bar{\nu}_e$ on light clusters. Neutral current neutrino scattering processes involving light clusters are omitted here included in the collision integral of the Boltzmann equation based on the coherent scattering formalism of Ref. [36]. However, the contribution of coherent scattering on all neutron rich light clusters to the inverse neutrino mean-free path is negligible [2]. Instead, this channel is dominated by neutrino-nucleon scattering above scattering on light clusters, by several orders of magnitude in the high density region where these light clusters are most abundant

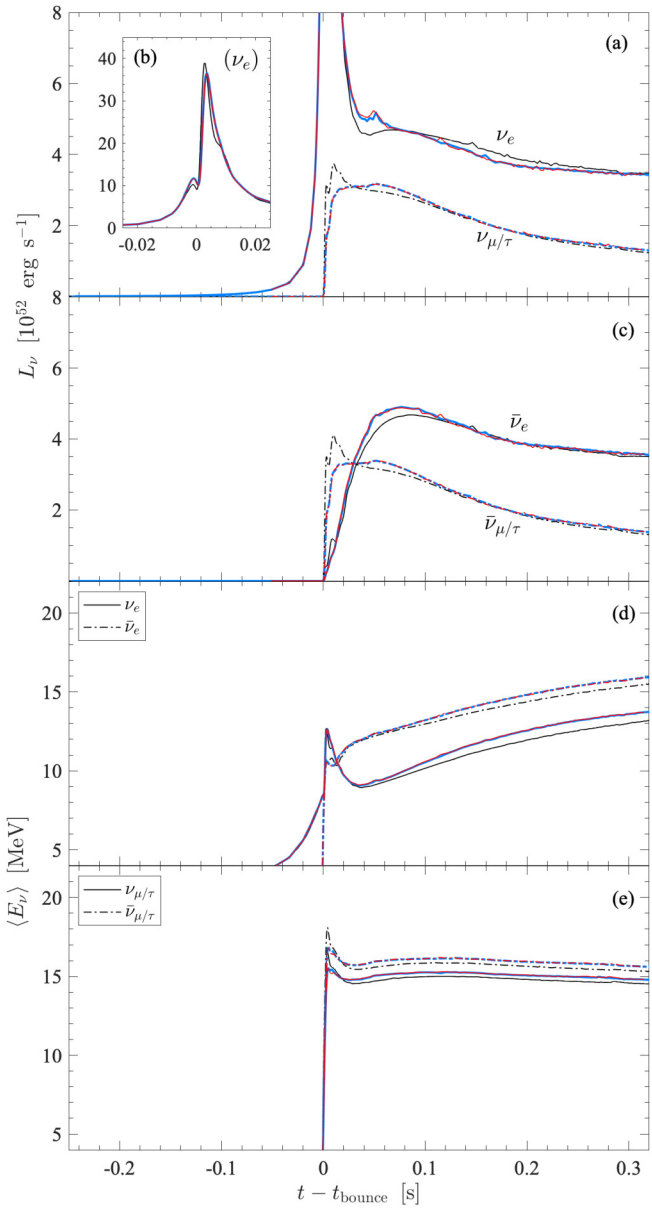

FIG. 10. Post bounce evolution of the neutrino luminosities, L_ν, for $(\nu_e, \nu_{\mu/\tau})$ in graph (a) and $(\bar{\nu}_e, \bar{\nu}_{\mu/\tau})$ in graph (c), and average energies, $\langle E_\nu \rangle$, for $(\nu_e, \bar{\nu}_e)$ in graph (d) and $(\nu_{\mu/\tau}, \bar{\nu}_{\mu/\tau})$ in graph (e), comparing the SN simulations based on the HS(DD2) EOS (black lines) and the generalized relativistic density-functional approach gDRF(DD2) without (blue lines) and with weak processes involving light clusters (red lines). Note that the latter two lay indistinguishably on top of each other (see text for details). The inlay graph (b) shows a zoom in the ν_e deleptonization burst.

(see Figs. 6–8). Hence, here we focus on charged current absorption processes.

A. Charged current weak rates with light clusters

The reaction rates involving light clusters with $1 < Z < 2$ and $2 < A < 4$ are provided in Appendix C1–C4. In the following the opacity expressions for ν_e and $\bar{\nu}_e$ absorption on ^{2}H [Eq. (C17)], inverse electron/positron captures on ^{2}H [Eq. (C28)], ν_e absorption on ^{3}H (C30), ν_e absorption on ^{3}He [Eq. (C34)] are being evaluated at two representative conditions (A) and (B) listed in Table III. The corresponding thermodynamic state is lso given in Table III, listing the mass fractions for the unbound nucleons and for the light clusters as well as their mean-field potentials. The corresponding weak rates involving these light nuclei are shown in Fig. 11 for the selected conditions (a) and (b). Besides the standard charged current reactions involving the unbound nucleons, for the processes involving ^{2}H the rate expressions are derived in Appendix C1 and Appendix C2 for the cross sections provided in Ref. [76], see also Ref. [78]. For the remaining momentum and angular integrals a 64-point and 32-point Gauss-Legendre numerical integration scheme is implemented, respectively. For the reactions involving ^{3}H and ^{3}He the bound state to bound state transitions are employed here (see Appendix C3), which are favored, due to the small Q-value of $m_{^3\rm H} - m_{^3\rm He} = 0.529$ MeV (including electron contributions), above the spallation reactions. The latter processes, transition into the continuum with three final state nucleons, are strongly suppressed due to the large Q values, 8.44 MeV (for ν_e) and 9.7 MeV (for $\bar{\nu}_e$), besides the three-body kinematics which further reduces the rates. Furthermore, the corresponding matrix element for the reactions involving ^{3}H and ^{3}He is well known from the triton decay.

In addition we also consider charged current processes with ^{4}H and ^{4}He (see Appendix C4), for which also only the bound state to bound state transitions are employed with a large Q value, $m_{^4\rm H} - m_{^4\rm He} = 22.7$ MeV, which is modified due to the mean-field potential differences. The latter contributions, $U_{^4\rm H} - U_{^4\rm He}$, can be large for these reactions at the conditions of interest here (see Table III). Furthermore, ^{4}H is unstable under laboratory conditions, it decays via the emission of a neutron to triton on the strong-interaction timescale. However, the presence of the nuclear medium enables the following strong equilibrium, $^3\mathrm{H} + \mathrm{n} \leftrightarrows {}^4\mathrm{H}$, which yields a finite abundance of ^{4}H. The same applies to all other neutron rich hydrogen and helium isotopes which are also unstable due to neutron emission under vacuum conditions, except ^{6}He which beta-decays to ^{6}Li. Details about the properties of ^{4}H, as well as all other neutron-rich hydrogen and helium isotopes, and how to implement medium modifications was discussed above

TABLE II. Neutrino reactions with light nuclei considered, including references for the corresponding cross sections.

	Weak process	Reference
1	$\nu_e + {}^2\mathrm{H} \rightleftarrows p + p + e^-$	[76]
2	$\bar{\nu}_e + {}^2\mathrm{H} \rightleftarrows n + n + e^+$	[76]
3	$\nu_e + n + n \rightleftarrows {}^2\mathrm{H} + e^-$	[2,76,77]
4	$\bar{\nu}_e + p + p \rightleftarrows {}^2\mathrm{H} + e^+$	[2,76,77]
5	$\nu_e + {}^3\mathrm{H} \rightleftarrows {}^3\mathrm{He} + e^-$	[2,77]
6	$\bar{\nu}_e + {}^3\mathrm{He} \rightleftarrows {}^3\mathrm{H} + e^+$	[2,77]
7	$\nu_e + {}^4\mathrm{H} \rightleftarrows {}^4\mathrm{He} + e^-$	This work
8	$\bar{\nu}_e + {}^4\mathrm{He} \rightleftarrows {}^4\mathrm{H} + e^+$	This work

TABLE III. Two thermodynamic conditions (A) and (B), as well as the corresponding mass fractions, X_i, and mean-field potentials, U_i, for the unbound nucleons and the light clusters.

	T [MeV]	ρ [g cm^{-3}]	Y_e	X_n	X_p	$X_{^2\mathrm{H}}$	$X_{^3\mathrm{H}}$	$X_{^4\mathrm{H}}$	$X_{^3\mathrm{He}}$	$X_{^4\mathrm{He}}$	U_n [MeV]	U_p [MeV]	$U_{^2\mathrm{H}}$ [MeV]	$U_{^3\mathrm{H}}$ [MeV]	$U_{^4\mathrm{H}}$ [MeV]	$U_{^3\mathrm{He}}$ [MeV]	$U_{^4\mathrm{He}}$ [MeV]
(A)	5	5×10^{12}	0.2	0.5	0.025	0.073	0.069	0.075	0.004	0.036	−1.5	−3.3	−3.0	−0.85	−1.9	−4.9	−2.3
(B)	7	2×10^{13}	0.05	0.8	0.001	0.004	0.003	0.0014	0.0003	0.0009	−6.3	−4.5	−10.02	0.77	14.7	−25.0	−15.2

in Sec. III. Important for the neutrino response involving these nuclei is the fact that a weak interaction matrix element for the charged current transitions is presently unknown, both experimentally for the obvious reason but also theoretically. To study their potential role on the neutrino emission as well as heating and cooling in SN simulations, we assume a Gammow-Teller transition amplitude. Similar as for the reactions involving ^{3}H and ^{3}He for which the transition amplitude is known from the triton decay, for reactions involving ^{4}H and ^{4}He we derive the weak transition amplitude from the thermally averaged cross sections for $\bar{\nu}_e$ absorption on ^{4}He of Ref. [79]. Details, including the cross sections, are given in Appendix C4.

Figure 11 compares the charged current opacity, χ_ν, for all charged current weak processes listed in Table II involving light nuclei with those of the unbound nucleons, for ν_e (top panels) and $\bar{\nu}_e$ (bottom panels), at two selected conditions (A) and (B) listed in Table III. They correspond roughly to regions in a core collapse SN simulation where light clusters are most abundant, in particular where the light cluster abundances exceed the abundance of protons, as listed in Table III. Here it becomes evident that at any of these conditions the reaction

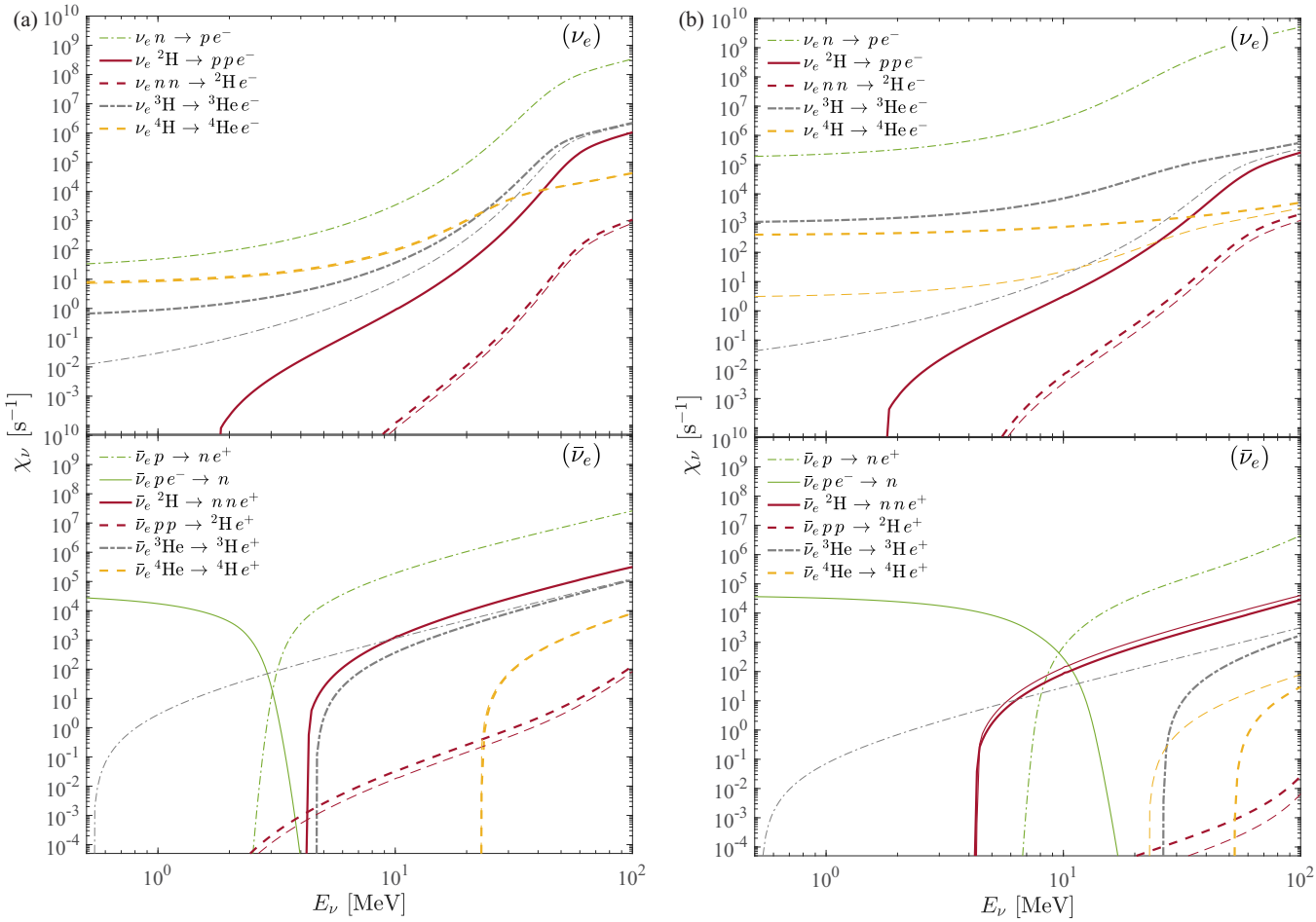

FIG. 11. Charged current neutrino (top panels) and antineutrino opacity (bottom panels) comparing the processes with the unbound nucleons (green dash-dotted lines) including the inverse neutron decay (green solid lines) for $\bar{\nu}_e$, and (anti)neutrino absorption on ^{2}H (solid dark red lines) as well as the inverse $e^\pm$ captures on ^{2}H (dark red dashed lines), (anti)neutrino absorption on ^{3}H and ^{3}He (gray dash-dotted lines), and (anti)neutrino absorption on ^{4}H and ^{4}He (yellow dashed lines), for the two selected conditions (A) in graph (a) and (B) in graph (b) as listed in Table III in the left and right panels, respectively. Thick lines include all medium modifications, see therefore the rate expressions in Appendix C, while thin lines omit them.

rates with the unbound nucleons largely exceed those of the light clusters (see Fig. 11). Note the opacity dropping to zero, which corresponds roughly to the medium-modified Q values which are a sharp threshold for the reactions treated within the elastic approximation, i.e., involving ^{3}H and ^{3}He as well as ^{4}H and ^{4}He. The mean-field potentials for these nuclei are given in Table III. They are provided by the gRDF(DD2) EOS.

B. SN simulations with weak reactions involving light clusters

All charged current weak reactions listed in Table II are implemented into the transport module of AGILE-BOLTZTRAN, based on the explicit rate expressions for the neutrino emissivity and opacity as given in Appendix C1–C5. We use the same neutrino transport discretization as before. The core collapse SN simulations employ then the new gRDF(DD2) EOS, which provide now also the information about the mean-filed potentials for all light clusters. These enter explicitly all rate expressions (see Appendix C1–C5).

The bulk evolution, from the shock formation up to several hundreds of ms post bounce, proceeds indistinguishable from the reference setup without considering weak reactions with light nuclei, as shown in Fig. 9. The impact from the additional weak reactions involving light clusters to the neutrino heating and cooling is generally small, as illustrated in Fig. 12(b) at 100 ms post bounce. In particular the contribution to the neutrino heating, which was suggested previously [11] where neutrino emission contributions were neglected which violates the relation of detailed balance, could not be found. Instead, the inclusion of weak reactions with light clusters leaves a negligible impact on the overall post bounce evolution, as illustrated in the evolution of the neutrinospheres in Fig. 9 as well as the neutrino luminosities and average energies in Fig. 10, in comparison to the simulations with gRDF(DD2) omitting weak reactions with light clusters.

This negligible impact on the post bounce evolution can be understood through the analysis of the neutrino heating/cooling rates, shown in the top panels of Fig. 12(b) at about 100 ms post bounce, for ν_e (left panel) and $\bar{\nu}_e$ (right panel). The comparison between the two SN simulations employing the gRDF(DD2) EOS without (solid blue lines) and with weak reactions involving light clusters (dashed red lines) reveals only minor differences. These are attributed not to additional heating and cooling contributions stemming from weak reactions with light clusters, but rather a slight mismatch of the timing between these two simulations on the order of 10 ms. Note the steep rise of the heating rates toward higher densities, which is due to the fact that the AGILE-BOLTZTRAN finite differencing scheme is not specially tuned to enforce the diffusion limit, for which the net rates would be zero (details can be found in Ref. [42]).

At the conditions where the neutrinos decouple, see therefore the locations of the accretion shock (vertical solid black lines) and of the neutrinospheres (vertical dashed black lines), the abundances of all neutron-rich light clusters are negligible in comparison to the abundances of the unbound nucleons. Consequently, the inverse mean-free path, shown in the bottom panels of Fig. 12(b), for ν_e (left panels) and $\bar{\nu}_e$ (right panels), are dominated by weak reactions involving the unbound nucleons. Note that the definition of the inverse mean-free path is given in Ref. [80], for which the neutrino phase-space integration is performed numerically using the neutrino distributions obtained from the SN simulations, following our previous works [31,81]. In addition to the charged current absorption reactions for ν_e and $\bar{\nu}_e$ (green dash-dotted lines), we also include the elastic neutrino-nucleon scattering processes (solid blue lines). The latter dominates the inverse mean-free path for $\bar{\nu}_e$. Note that for $\bar{\nu}_e$ the inverse mean-free path for the inverse electron captures on ^{2}H (dashed red line) is below the scale of the plot. The situation remains the same also at later times.

Only toward higher density, in excess of few times 10^{13} g cm^{-3}, there are contributions from weak interactions with light clusters, in particular involving ^{2}H. This is related with the increasing abundances of all light clusters toward higher densities, as illustrated and discusses above in Sec. IV. However, first, their contribution remains negligible, and second, at these high densities the entire neutrino spectrum is trapped such that it leaves no impact on the post bounce evolution. The situation may change when the neutrinospheres shift to higher densities during the PNS deleptonization after the SN explosion onset has been launched and the nascent PNS deleptonizes and cools via the emission of neutrinos of all flavors, which remains to be explored in the future.

VI. SUMMARY

The present article introduces the gRDF(DD2) EOS for astrophysical simulations. Particular focus is devoted to the improved description of light and heavy nuclear clusters, taking consistently into account medium modifications of the nuclear binding energies with contributions due to Pauli blocking and Coulomb corrections. The gRDF(DD2) EOS includes self consistently neutron-rich hydrogen ($A = 2$–7) and helium isotopes ($A = 3$–8), some of which are weakly bound such as the hydrogen isotopes with $A > 3$ as well as ^{5}He, and were hence omitted previously. Their role was recently overestimated due to the implementation of the NSE approach [14] which is based on vacuum binding energies. This caveat has been overcome within the present work taking explicitly into account individual scattering state contributions following the QS approach of Ref. [17], which solves the in-medium Schrödinger equation. We find that the continuum contributions, known as virial corrections, provide the essential contributions to all weakly bound clusters such as ^{4}H and ^{5}He, while they play only a minor role for the bound clusters such as ^{3}H, ^{3}He and ^{4}He. For ^{2}H the virial corrections are known to have contributions already at low densities [61,82].

While the QS framework allows for the calculations of individual light clusters, it cannot be applied for astrophysical EOS which require the inclusion of more than 1000 nuclear species, in particular also heavy nuclei. Therefore, the gRDF approach has been developed here, which is based on the nuclear in-medium binding energies provided for selected light nuclear clusters from the QS calculations. Consequently, gRDF results in good quantitative agreement with the quantum-statistical approach in terms of the properties of

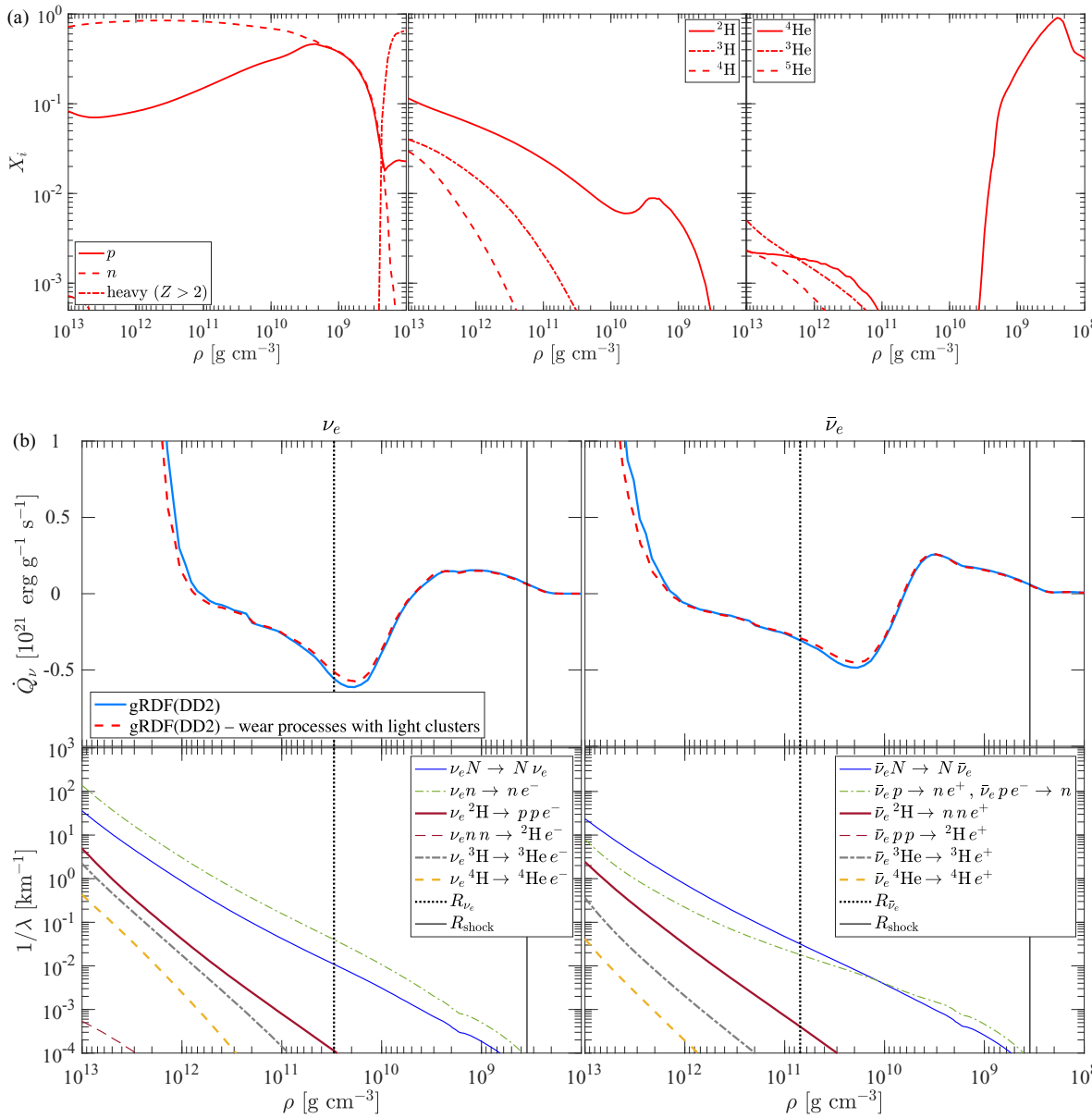

FIG. 12. SN simulation profiles with respect to the restmass density at 100 ms post bounce. Graph (a): mass fractions, X_i, for selected nuclear species. Graph (b): net neutrino heating rate, $\dot{Q}_\nu$, comparing gRDF(DD2) with (red dashed lines) and without (solid light blue lines) weak reactions involving light nuclei for ν_e (left panel) and $\bar{\nu}_e$ (right panel), as well as the inverse neutrino mean-free path, $1/\lambda$, for selected weak processes corresponding to the simulations with the gRDF(DD2) EOS including weak reactions with light clusters, also for ν_e (left panel) and $\bar{\nu}_e$ (right panel), distinguishing neutral current neutrino-nucleon scattering (solid blue lines), charged current neutrino absorption with unbound nucleons (dark green dash-dotted lines), ^{2}H (thick solid dark red lines), inverse $e^\pm$ captures on ^{2}H (thin dashed dark red lines), involving ^{3}H and ^{3}He (thick gray dash-dotted lines) as well as ^{4}H and ^{4}He (thick dashed dark yellow lines). The vertical black lines mark the locations of the neutrinospheres (dotted lines) and the shock position (solid lines).

the light nuclear clusters. Deviations are observed only for the weakly bound light clusters. In particular, both approaches gRDF and QS predict the dissolving of the light nuclear clusters at substantially lower density, already at about one-tenth of the nuclear saturation density, than the NSE approach of Ref. [9], which implements an excluded volume mechanism instead. A qualitative comparison of the NSE based excluded volume approach and the QS can be found in Ref. [83]. Here, gRDF provides the general description for all clusters where the heavy clusters, defined as $Z > 2$, are taken into account following Ref. [24]. This results in the presence of heavy clusters up to high densities, on the order of the saturation density, and hence a late transition to homogeneous matter.

These aspects of the description of light and heavy clusters significantly improve the commonly employed approaches, not only the excluded volume of Ref. [9] based on NSE but also the single-nucleus approximation employed [6,7,84] featuring a phase transition construction for the transition to homogeneous matter, the Thomas-Fermi approximation [8,20] and the spherical Wigner-Seitz cell approach [62].

We implement the new gRDF(DD2) EOS into our spherically symmetric core collapse SN model AGILE-BOLTZTRAN and perform SN simulations, launched from the 18 $M_\odot$ progenitor [73]. In comparison with the HS(DD2) NSE EOS we find a substantially different composition, particularly significantly lower abundances of all light clusters and the presence of ^{4}H and ^{5}He which were omitted in previous SN simulations. Furthermore, toward high densities at the PNS interior, the abundances of ^{5}He exceed those of ^{3}He and ^{4}He due to the generally neutron-rich conditions with low $Y_e = 0.1$–0.25. This is also the reason for the high yields of ^{3}H and ^{4}H, being comparable to those of unbound protons. Furthermore, the heavy cluster abundance at high densities has a strong softening impact on the PNS structure, already around the stellar core bounce, which in turn results in lower central densities and higher temperatures. Also the emission of the ν_e deleptonization burst, associated with the bounce shock propagation across the ν_e sphere, is affected by the presence of more heavy clusters, featuring a lower abundance of unbound nucleons and hence a slight reduction of the magnitude as well as a minor broadening. Furthermore, the generally softer high-density behavior of the gRDF(DD2) EOS results in a faster shock retreat and a smaller shock radius during the post bounce evolution up to several hundreds of milliseconds. It affects the post bounce neutrino emission, with generally higher average neutrino energies.

The spherically symmetric simulations presented here, featuring a faster shock retreat due to the softer gRDF(DD2) EOS, in comparison to the HS(DD2) EOS, result in less favorable conditions for shock revival in terms of neutrino heating. However, similar comparisons in the multidimensional SN framework indicate the opposite effect with respect to shock revival via neutrino heating [3,47,85–89]. This remains to be explored in multidimensional SN simulations.

The gRDF(DD2) EOS provides not only the gross thermodynamics properties of heavy and light nuclear clusters but also the microscopic quantities such as scalar and vector self energies for the unbound nucleons and for all light clusters. The latter enables us to consistently treat a variety of weak processes with light clusters, which were either omitted in previous core collapse SN studies or crudely approximated. While it has been shown previously that neutral current scattering reactions involving light clusters are negligible, instead this channel is dominated by neutrino scattering off unbound nucleons, here we focus on the charged current absorption reactions. We introduce the explicit rate expressions for the spallation reactions for ^{2}H as well as electron/positron captures on ^{2}H, based on the cross sections of Ref. [76]. Further reaction rates involving ^{3}H and ^{3}He as well as ^{4}H and ^{4}He are provided based on the elastic approximation where we consider the bound state to bound state transition since the transitions into the continuum are negligible [2]. These charged current weak rates are implemented into the collision integral of AGILE-BOLTZTRAN and additional SN simulations are performed. The comparison with the gRDF(DD2) EOS reference case, where these weak processes were omitted, show a negligible impact from the inclusion of weak reactions with these light clusters. Nevertheless, we would like to stress the demand for more sophisticated calculations of charged current neutrino absorption cross sections for the neutron-rich nuclei introduced here, in particular taking into account the broad width of all neutron-rich hydrogen isotopes, nuclear structure effects for the vacuum-stable nuclei, e.g., ^{4}He and ^{6}He as well as generally final-state and medium contributions.

ACKNOWLEDGMENTS

The authors appreciate the hospitality of the GSI Helmholtzzentrum für Schwerionenforschung and in particular Thomas Neff for stimulating discussions. T.F. and N.U.F.B. acknowledge support from the Polish National Science Center (NCN) under Grants No. 2016/23/B/ST2/00720 (T.F.), No. 2019/33/B/ST9/03059 (T.F.), and No. 2019/32/C/ST2/00556 (N.U.F.B.). The supernova simulations are performed at the Wroclaw Center for Scientific Computing and Networking (WCSS) in Wroclaw (Poland).

APPENDIX A: gRDF RELATIVISTIC MEAN-FIELD MODEL REVISITED

All EOS quantities that are relevant for SN simulations can be derived from the grand canonical potential density, ω, of the gRDF model. It depends on the temperature, T, and the set of chemical potentials, $\{\mu_i\}$, of all considered particles. In this formulation chosen here, meson fields of the RMF model do not appear explicitly and only baryons are considered as effective degrees of freedom. Then the grand canonical potential density can be written as follows:

$$\omega(T, \{\mu_i\}) = \sum_{i\in\mathcal{B}} \omega_i + \omega_{\rm meson} - \omega^{(r)}, \tag{A1}$$

with contributions from baryons, $\mathcal{B} = \{n, p, {}^2\mathrm{H}, {}^3\mathrm{H}, \dots\}$, i.e., nucleons and nuclei, ω_i, as well as mesons $\omega_{\rm meson}$ and rearrangement terms denoted as $\omega^{(r)}$. The baryons are treated as quasiparticles with effective chemical potentials $\mu_i^* = \mu_i - \Sigma_i^V$ and with the dispersion relation,

$$E_i(p, m_i^*) = \sqrt{p^2 + (m_i^*)^2}, \tag{A2}$$

depending on the momentum p and the effective mass $m_i^* = m_i - \Sigma_i^S$. The quantities Σ_i^V and Σ_i^S are the vector and scalar self-energies or potentials of the baryons, see below, and m_i is the rest mass in vacuum. The particle number and scalar densities are defined by the standard expressions

$$n_i = -\left.\frac{\partial\omega}{\partial\mu_i}\right|_{T,\{\mu_{j\neq i}\}}, \quad n_i^{(s)} = \left.\frac{\partial\omega}{\partial m_i}\right|_{T,\{\mu_j\}} \tag{A3}$$

as derivatives of ω with respect to the chemical potentials μ_i and masses m_i, respectively. The contribution of baryons to the total grand canonical potential density Eq. (A1) has the form

$$\omega_i^{(0)}(T, m_i^*, \mu_i^*) = -T\frac{g_i(T)}{\sigma_i}\int\frac{d^3p}{(2\pi)^3} \times \ln\left\{1 + \sigma_i \exp\left[-\frac{E_N(p, m_i^*) - \mu_i^*}{T}\right]\right\}, \tag{A4}$$

with particle degeneracy factors g_i that depend on temperature in the case of heavy nuclei to take the contribution of excited states into account. The quantity σ_i encodes the particle statistics (Fermi-Dirac: $\sigma_i = +1$, Bose-Einstein: $\sigma_i = -1$). For heavy nuclei, the nonrelativistic limit of the energy, $E_i = m_i + p^2/(2m_i)$, and Maxwell-Boltzmann statistics are assumed, i.e., the limit $\sigma_i \to 0$ is taken in Eq. (A4). The meson contribution,

$$\omega_{\rm meson} = -\tfrac{1}{2}\left(C_\omega n_\omega^2 + C_\rho n_\rho^2 - C_\sigma n_\sigma^2\right), \tag{A5}$$

to Eq. (A1) is expressed with the help of the coupling factors $C_j = \Gamma_j^2/m_j^2$ of the mesons $j \in \mathcal{M} = \{\omega, \rho, \sigma\}$ and their source densities n_j. The couplings Γ_j depend on the total baryon density $n_B = \sum_{i\in B} B_i n_i$ with baryon numbers B_i and baryon number densities n_i. The density dependence of the couplings causes the appearance of a meson rearrangement term

$$V_{\rm meson}^{(r)} = \tfrac{1}{2}\left(C'_\omega n_\omega^2 + C'_\rho n_\rho^2 - C'_\sigma n_\sigma^2\right), \tag{A6}$$

with derivatives $C'_j = dC_j/dn_B$ in the vector potential

$$\Sigma_i^V = C_\omega g_{i\omega} n_\omega + C_\rho g_{i\rho} n_\rho + B_i V_{\rm meson}^{(r)} + W_i^{(r)} \tag{A7}$$

besides the usual meson contributions in RMF models and a further rearrangement term,

$$W_i^{(r)} = \sum_{j\in\mathcal{B}} n_j^{(s)} \frac{\partial \Delta m_j}{\partial n_i}\,, \tag{A8}$$

due to the medium dependence of the masses. The scalar potential

$$\Sigma_i^S = C_\sigma g_{i\sigma} n_\sigma - \Delta m_i \tag{A9}$$

explicitly includes the medium dependent mass shift Δm_i for all baryons except nucleons. The degeneracy factors g_i as well as the factors g_{ij} in the vector and scalar potentials are specified Ref. [24]. The latter also appear in the source densities,

$$n_\omega = \sum_{i\in\mathcal{B}} g_{i\omega} n_i, \quad n_\rho = \sum_{i\in\mathcal{B}} g_{i\rho} n_i, \quad n_\sigma = \sum_{i\in\mathcal{B}} g_{i\sigma} n_i^{(s)}. \tag{A10}$$

The mass shifts $\Delta m_i = \Delta m_i^{(\rm Coul)} + \Delta m_i^{(\rm strong)}$ in the scalar potential contain a Coulomb contribution due to the screening of the Coulomb field of the nuclei by the charged leptons and a strong shift that arises from the action of the Pauli principle. It causes a blocking of states in the medium that are no longer available for the formation of nuclei as many-body correlations. The mass shifts depend on the particle densities and the temperature. Explicit expressions are given Ref. [24]. Finally, the last term in Eq. (A1) has the form

$$\omega^{(r)} = V_{\rm meson}^{(r)} n_B + \sum_{i\in\mathcal{B}} W_i^{(r)} n_i, \tag{A11}$$

with the contributions from the density dependence of the couplings and the mass shifts. The rearrangement terms in all quantities are essential for the thermodynamic consistency of the model and lead to the standard expressions for the densities of the quasiparticles,

$$n_i = g_i \int \frac{d^3p}{(2\pi)^3}\, f_i, \quad n_i^{(s)} = g_i \int \frac{d^3p}{(2\pi)^3}\, f_i\, \frac{m_i^*}{E_i}, \tag{A12}$$

with the distribution function

$$f_i(T, p, m_i^*, \mu_i^*) = \left\{\exp\left[\frac{E_i(p, m_i^*) - \mu_i^*}{T}\right] + \sigma_i\right\}^{-1}. \tag{A13}$$

The grand canonical potential density Eq. (A1) immediately gives the pressure $p = -\omega$ of the system and the free energy density, f, is found from the thermodynamic relation

$$f = -p + \sum_{i\in\mathcal{B}} \mu_i n_i. \tag{A14}$$

The entropy density, s, is obtained from the standard definition as

$$s = -\left.\frac{\partial\omega}{\partial T}\right|_{\{\mu_i\}} = -\sum_{i\in\mathcal{B}} g_i \int \frac{d^3p}{(2\pi)^3} \times \left[f_i \ln f_i + \frac{1-\sigma_i f_i}{\sigma_i} \ln\left(1-\sigma_i f_i\right)\right] - \sum_{i\in\mathcal{B}} \frac{\omega_i^{(0)}}{g_i} \frac{\partial g_i}{\partial T}, \tag{A15}$$

with an contribution that originates from the temperature dependence of the degeneracy factors of nuclei.

APPENDIX B: VIRIAL EXPANSION AND GENERALIZED BETH-UHLENBECK EQUATION

Within a consistent QS approach, the densities of nucleons (as function of T and the chemical potentials, e.g., of the neutron μ_n and the proton μ_p) are decomposed into partial densities of different channels $\{A, Z\}$ which contain the bound states (ground state and excited states) of the nucleus with mass number A and proton number Z, as well as the continuum states. As example, in the ^{2}H channel we obtain the generalized Beth-Uhlenbeck equation as follows (for details, see Ref. [60]),

$$n_{^2\rm H}(T, \mu_n, \mu_p) = \frac{3}{(\pi\hbar^2/mT)^{3/2}} \exp\left(\frac{\mu_n + \mu_p}{T}\right) \times \left\{\left[\exp\left(-\frac{E_{^2\rm H}}{T}\right) - 1\right] + \frac{1}{\pi T}\int_0^\infty dE \exp \times \left(-\frac{E}{T}\right)\left[\delta_{p,n}(E) - \frac{1}{2}\sin\left(2\delta_{p,n}(E)\right)\right]\right\}. \tag{B1}$$

The two-nucleon bound state $E_{^2\rm H}$ and phase shifts $\delta_{p,n}$ are solutions of an in-medium two-nucleon Schrödinger equation which is derived from a Green's function approach. In contrast to the simple Beth-Uhlenbeck equation where the deuteron bound state energy $E_{^2\rm H}^{(0)} = -2.225$ MeV appears, the medium modified binding energy is taken. The phase shifts $\delta_{p,n}(E)$ are also modified by in-medium effects such as self-energy and Pauli-blocking terms. Because the single-nucleon contribution contains already the quasiparticle shift, e.g., within the

gRDF(DD2) approach, the sin-term in the continuum contribution appears to avoid double counting.

Calculations show that the simple ground-state contribution to the partial density is reduced if the continuum contributions are taken into account. This reduction, which increases with increasing T, is well-known from the virial expansion of the EOS. We can express the reduction introducing the effective cluster energy $E^{\rm eff}_{^2{\rm H}}$ as

$$n_{^2{\rm H}}(T,\mu_n,\mu_p) = \frac{3}{(\pi\hbar^2/mT)^{3/2}} \exp\left(-\frac{E^{\rm eff}_{^2{\rm H}} - \mu_n - \mu_p}{T}\right), \tag{B2}$$

which now becomes temperature and density dependent. Within a more detailed description, the cluster quasiparticle energy is also depending on the center of mass momentum P so that the integral over P is not expressed by the thermal wave length but has to be performed explicitly. In the low-density limit, using the n-p scattering data, the values for the second virial coefficient $b_{pn}(T)$ are given in Ref. [61]. The effective binding energy follows as

$$B^{\rm eff}_{^2{\rm H}}(T) = -E^{\rm eff}_{^2{\rm H}}(T) = -T \ln\left[\frac{\sqrt{2}}{3} b_{pn}(T)\right]. \tag{B3}$$

Similarly, ^{4}H and ^{5}He can be treated this way. In both cases, no bound states exist, and only the integral over the scattering states remains in Eq. (B1). The chemical potentials contain the number of neutrons and protons, respectively, of the cluster, and the bound state energies of the scattered (^{4}H, ^{4}He) must be added. An effective cluster energy $E^{\rm eff}_{A,Z}$ can be introduced which is also strongly dependent on T but also on the density. Details are given in Ref. [17], where also analytical expressions for the T, ρ dependence of $E^{\rm eff}_{A,Z}$ for ^{4}H and ^{5}He are given. These quantities are shown in Fig. 1. In the low-density limit, for ^{5}He we consider

$$b_{\alpha n}(T) = \left(\frac{5}{4}\right)^{3/2} \frac{1}{\pi T} \int_0^\infty dE\, e^{-E/T} \delta_{\alpha n}(E), \tag{B4}$$

which is also considered in Ref. [61]. The effective cluster energy follows as

$$E^{\rm eff}_{^5{\rm He}}(T) = E_{^5{\rm He}} - T \ln\left[\frac{4}{5^{3/2}} b_{\alpha n}(T)\right]. \tag{B5}$$

For ^{4}H, the virial expression and the corresponding effective cluster energy in the low-density limit follow from the $^3{\rm H} - n$ scattering data [82].

APPENDIX C: WEAK PROCESSES INVOLVING LIGHT CLUSTERS

The novel weak reactions involving light clusters with $1 < Z < 2$ are listed in Table II. To include this set of charged current weak processes into the collision integral of the Boltzmann equation of `AGILE-Boltztran`,

$$\left.\frac{1}{c}\frac{df_\nu}{dt}\right|_{\rm collisions}(E_\nu,\mu) = j_\nu(E_\nu)[1 - f_\nu(E_\nu,\mu)] - \chi_\nu(E_\nu) f_\nu(E_\nu,\mu), \tag{C1}$$

with incoming neutrino distribution $f_\nu(E_\nu,\mu)$ depending on the incoming neutrino energy E_ν as well as on the neutrino scattering angle $\mu = \sin\vartheta$ (for illustration, see Fig. 1 in Ref. [33]), the total neutrino emissivity j_ν and opacity χ_ν are supplemented by those of the reactions listed in Table II,

$$j_{\nu_e} = j_{\nu_e n} + j_{\nu_e\,^2{\rm H}} + j_{\nu_e nn} + j_{\nu_e\,^3{\rm H}} + j_{\nu_e\,^4{\rm H}},$$
$$\chi_{\nu_e} = \chi_{\nu_e n} + \chi_{\nu_e\,^2{\rm H}} + \chi_{\nu_e nn} + \chi_{\nu_e\,^3{\rm H}} + \chi_{\nu_e\,^4{\rm H}}, \tag{C2a}$$
$$j_{\bar\nu_e} = j_{\bar\nu_e p} + j_{\bar\nu_e\,^2{\rm H}} + j_{\bar\nu_e pp} + j_{\bar\nu_e\,^3{\rm He}} + j_{\bar\nu_e\,^4{\rm He}},$$
$$\chi_{\bar\nu_e} = \chi_{\bar\nu_e n} + \chi_{\bar\nu_e^2{\rm H}} + \chi_{\bar\nu_e pp} + \chi_{\bar\nu_e\,^3{\rm He}} + \chi_{\bar\nu_e\,^4{\rm He}}, \tag{C2b}$$

where the individual emissivities and opacities are related via the relation of detailed balance (Appendix C 5). In the following sections the derivation of these reaction rates is provided.

1. Absorption of ν_e and $\bar\nu_e$ on ^{2}H

For the following weak processes with deuteron,

$$\nu_e + {}^2{\rm H} \to p + p + e^-, \quad \bar\nu_e + {}^2{\rm H} \to n + n + e^+, \tag{C3}$$

we can introduce relative and center-of-mass momenta,

$$\mathbf{P} = \mathbf{p}_1 + \mathbf{p}_2, \quad \mathbf{p} = \frac{\mathbf{p}_1 - \mathbf{p}_2}{2}, \tag{C4}$$

with individual nucleon momenta, $\mathbf{p}_1$ and $\mathbf{p}_2$, and express energy and momentum conservation in these coordinates as follows:

$$\mathbf{p}_\nu + \mathbf{p}_{^2{\rm H}} = \mathbf{p}_e + \mathbf{P},$$
$$E_\nu + \frac{\mathbf{p}_\nu^2}{2m_{^2{\rm H}}} + m_{^2{\rm H}} = E_e + \frac{\mathbf{P}^2}{4m_p} + \frac{\mathbf{p}^2}{m_p} + 2m_p. \tag{C5}$$

Here we replace the effective masses with the vacuum masses since $1/m^*_{^2{\rm H}} \simeq 1/m_{^2{\rm H}}$ and $1/m^*_N \simeq 1/m_N$. In the calculations of the differential cross sections in Ref. [76], the authors neglects the dependence of the cross section on the direction of $\mathbf{p}$, they compute an angle-averaged value. For the neutrino transport, we need to recover the dependence of the cross-section on the direction of $\mathbf{p}$. For convenience we will define it with respect to the direction of the vector $\mathbf{P}$, for which we define the angle θ such that $\mathbf{p}\cdot\mathbf{P} = pP\cos\theta$ and the differential cross section is given as follows:

$$\frac{d\sigma_{\nu\,^2{\rm H}}}{d(\cos\theta)d\Omega_e dp_e}(E_\nu) = \frac{1}{2}\frac{d\sigma_{\nu\,^2{\rm H}}}{d\Omega_e dp_e}(E_\nu), \tag{C6}$$

with the assumption of isotropy.

The general expression for the reaction rates for the charged current absorption processes with deuteron, break-up reactions (1) and (2) in Table II, is given by the following integral equation,

$$\chi_{\nu\,^2{\rm H}}(E_\nu) = \frac{2\pi G^2}{\hbar c} g_{^2{\rm H}} \int \frac{d^3p_{^2{\rm H}}}{(2\pi\hbar c)^3}\frac{d^3p_e}{(2\pi\hbar c)^3}\frac{d^3p_1}{(2\pi\hbar c)^3}\frac{d^3p_2}{(2\pi\hbar c)^3} \times \tilde f_{^2{\rm H}}(E_{^2{\rm H}})[1 - f_e(E_e)][1 - f_1(E_1)][1 - f_2(E_2)] \times (2\pi\hbar c)^3 |M|^2 \delta^4(p_\nu + p_{^2{\rm H}} - p_e - p_1 - p_2), \tag{C7}$$

with the product of the Fermi coupling constant, G_F, and the ud entry of the Cabibbo-Kobayashi-Maskawa matrix, denoted as $G = G_F V_{ud}$, with the Fermi-Dirac equilibrium distribution functions f_i, except the Bose-Einstein distribution function

$\tilde{f}_{^2\mathrm{H}}$ for deuteron, as well as with spin averaged interaction matrix element M which connects initial and final states. In the zero-momentum exchange approximation, $\mathbf{q} = \mathbf{p}_\nu - \mathbf{p}_e$ with $q \simeq 0$, Eq. (C7) reduces to the following form:

$$\chi_{\nu\,^2\mathrm{H}}(E_\nu) = \frac{2\pi G^2}{\hbar c} g_{^2\mathrm{H}} \int \frac{d^3p_{^2\mathrm{H}}}{(2\pi\hbar c)^3} \frac{d^3p_e}{(2\pi\hbar c)^3} \frac{d^3P}{(2\pi\hbar c)^3} d^3p\, |M|^2 \tilde{f}_{^2\mathrm{H}}(E_{^2\mathrm{H}})[1 - f_e(E_e)][1 - f_1(E_1)][1 - f_2(E_2)] \tag{C8}$$

$$\times \delta(E_\nu + E_{^2\mathrm{H}} - E_e - E_1 - E_2)\delta^3(\mathbf{p}_{^2\mathrm{H}} - \mathbf{P}) \tag{C9}$$

$$= \frac{2\pi G^2}{\hbar c(2\pi\hbar c)^3} g_{^2\mathrm{H}} \int \frac{d^3p_{^2\mathrm{H}}}{(2\pi\hbar c)^3} \frac{d^3p_e}{(2\pi\hbar c)^3} 2\pi p^2\, d(\cos\theta)\, |M|^2 \tilde{f}_{^2\mathrm{H}}(E_{^2\mathrm{H}})[1 - f_e(E_e)][1 - f_1(E_1)][1 - f_2(E_2)], \tag{C10}$$

with

$$\mathbf{P} = \mathbf{p}_{^2\mathrm{H}}, \quad p = \sqrt{m_p(E_\nu - E_e + m_{^2\mathrm{H}} - 2m_p)}, \tag{C11a}$$

$$E_1 = \frac{1}{2m_p}\left(\frac{p_{^2\mathrm{H}}^2}{4} + p^2 + pp_{^2\mathrm{H}}\cos\theta\right) + m_p, \quad E_2 = \frac{1}{2m_p}\left(\frac{p_{^2\mathrm{H}}^2}{4} + p^2 - pp_{^2\mathrm{H}}\cos\theta\right) + m_p. \tag{C11b}$$

To relate the opacity with the double-differential cross section computed in Ref. [76] we use the following association:

$$\frac{d\sigma_{\nu\,^2\mathrm{H}}}{d(\cos\theta)d\Omega_e dp_e}(E_\nu) = \frac{2\pi\, G^2}{(\hbar c)(2\pi\hbar c)^6} 2\pi\,(p_e p)^2 |M|^2, \tag{C12}$$

and obtain the following expression for the opacity,

$$\chi_{\nu\,^2\mathrm{H}}(E_\nu) = g_{^2\mathrm{H}} \int \frac{d^3p_{^2\mathrm{H}}}{(2\pi\hbar c)^3} d\Omega_e dp_e d(\cos\theta)\left(\frac{d\sigma_{\nu\,^2\mathrm{H}}}{d(\cos\theta)d\Omega_e dp_e}(E_\nu^*)\right)\tilde{f}_{^2\mathrm{H}}(E_{^2\mathrm{H}})[1 - f_e(E_e)][1 - f_1(E_1)][1 - f_2(E_2)], \tag{C13}$$

with the medium-modified cross section due to the shifted neutrino energy E_ν^*, which can be obtained via the following equations,

$$E_{\nu_e}^* = E_{\nu_e} + (m_{^2\mathrm{H}}^* - m_{^2\mathrm{H}}) + U_{^2\mathrm{H}} - 2(m_p^* - m_p) - 2U_p, \tag{C14}$$

$$E_{\bar{\nu}_e}^* = E_{\bar{\nu}_e} + (m_{^2\mathrm{H}}^* - m_{^2\mathrm{H}}) + U_{^2\mathrm{H}} - 2(m_n^* - m_n) - 2U_n. \tag{C15}$$

The medium effects, i.e., the mean-field potentials and the effective masses, are provided by the gRDF(DD2) EOS. They also modify Eqs. (C11a)–(C11b) as follows:

$$p = \sqrt{m_p^*\left(E_\nu - E_e + m_{^2\mathrm{H}}^* - 2m_p^* + U_d - 2U_p\right)}, \tag{C16a}$$

$$E_1 = \frac{1}{2m_p^*}\left(\frac{p_{^2\mathrm{H}}^2}{4} + p^2 + pp_{^2\mathrm{H}}\cos\theta\right) + m_p^* + U_p, \quad E_2 = \frac{1}{2m_p^*}\left(\frac{p_{^2\mathrm{H}}^2}{4} + p^2 - pp_{^2\mathrm{H}}\cos\theta\right) + m_p^* + U_p. \tag{C16b}$$

Furthermore, since final state Pauli-blocking does not depend on the electron angular direction one can integrate the electron solid angle and obtain the final expression for the opacity for (anti)neutrino absorption on ^{2}H,

$$\chi_{\nu\,^2\mathrm{H}}(E_\nu) = \frac{g_{^2\mathrm{H}}}{2} \int \frac{d^3p_{^2\mathrm{H}}}{(2\pi\hbar c)^3} dp_e\, d(\cos\theta)\left(\frac{d\sigma_{\nu\,^2\mathrm{H}}}{dp_e}(E_\nu^*)\right)\tilde{f}_{^2\mathrm{H}}(E_{^2\mathrm{H}})\,(1 - f_e(E_e))[1 - f_1(E_1)][1 - f_2(E_2)], \tag{C17}$$

where we have used Eq. (C6). The remaining three integrals are evaluated computationally on flight in the SN simulation reported above in Sec. V.

2. $e^\pm$ captures on ^{2}H

In addition to the (anti)neutrino absorption on deuteron, we can also consider electron captures on deuteron,

$$e^- + {}^2\mathrm{H} \to n + n + \nu_e, \quad e^+ + {}^2\mathrm{H} \to p + p + \bar{\nu}_e, \tag{C18}$$

for which the differential cross section is given by the following expression:

$$\frac{d\sigma_{e\,^2\mathrm{H}}}{d\Omega_{\nu_e} dp_\nu}(E_e) = \frac{2\pi G^2}{2(\hbar c)(2\pi\hbar c)^6} 4\pi\, p_\nu^2 p(E_e, E_\nu)^2 |M|^2, \tag{C19}$$

with additional factor 2 due to the two internal degrees of freedom for the electron. In the following we will examine the reaction with electrons, for which we have the following settings:

$$\mathbf{P} = \mathbf{p}_{^2\mathrm{H}}, \quad p(E_e, E_{\nu_e}) = \sqrt{m_n(E_e - E_{\nu_e} + m_{^2\mathrm{H}} - 2m_n)}, \tag{C20a}$$

$$E_1 = \frac{1}{2m_n}\left(\frac{p_{^2\mathrm{H}}^2}{4} + p^2 + pp_{^2\mathrm{H}}\cos\theta\right) + m_n, \quad E_2 = \frac{1}{2m_n}\left(\frac{p_{^2\mathrm{H}}^2}{4} + p^2 - pp_{^2\mathrm{H}}\cos\theta\right) + m_n. \tag{C20b}$$

Furthermore, note that cross section Eq. (C19) can be related with the cross section for $\bar{\nu}_e$-absorption on deuteron (reaction (2) in Table II) as follows:

$$\frac{d\sigma_{\bar{\nu}_e\,^2\mathrm{H}}}{d\Omega_e dp_e}(E_{\bar{\nu}_e}) = \frac{2\pi G^2}{(\hbar c)(2\pi\hbar c)^6} 4\pi p_e^2 p(E_{\bar{\nu}_e}, E_e)^2 |M|^2, \tag{C21}$$

with

$$\mathbf{P} = \mathbf{p}_{^2\mathrm{H}}, \quad p(E_{\bar{\nu}_e}, E_e) = \sqrt{m_n(E_{\bar{\nu}_e} - E_e + m_{^2\mathrm{H}} - 2m_n)}, \tag{C22a}$$

$$E_1 = \frac{1}{2m_n}\left(\frac{p_{^2\mathrm{H}}^2}{4} + p^2 + pp_{^2\mathrm{H}}\cos\theta\right) + m_n, \quad E_2 = \frac{1}{2m_n}\left(\frac{p_{^2\mathrm{H}}^2}{4} + p^2 - pp_{^2\mathrm{H}}\cos\theta\right) + m_n. \tag{C22b}$$

Here we find the following relationship between the cross section for capturing an electron of energy E_e producing a ν_e of momentum p_{ν_e} and the cross section for $\bar{\nu}_e$-absorption of the same energy, $E_{\bar{\nu}_e} = E_e$ and producing a positron of momentum $p_e = p_{\bar{\nu}_e}$:

$$\frac{d\sigma_{e^-\,^2\mathrm{H}}}{d\Omega_{\nu_e} dp_{\nu_e}}(E_e) = \frac{1}{2}\frac{p(E_e, p_{\bar{\nu}_e})^2}{p(E_e, E_e(p_{\bar{\nu}_e}))^2}\frac{d\sigma_{\bar{\nu}_e\,^2\mathrm{H}}}{d\Omega_e dp_e}(E_e) \simeq \frac{1}{2}\frac{d\sigma_{\bar{\nu}_e\,^2\mathrm{H}}}{d\Omega_e dp_e}(E_e), \tag{C23}$$

assuming relativistic electrons. The ν_e-emissivity can be obtained from Eq. (C8) using the change $(1 - f_e) \to 2f_e$ to obtain after substituting the electron-capture cross section:

$$j_{e^-\,^2\mathrm{H}}(E_{\nu_e}) = \frac{g_{^2\mathrm{H}}}{2}\int \frac{d^3p_{^2\mathrm{H}}}{(2\pi\hbar c)^3} d(\cos\theta) d\Omega_e dp_e \left(\frac{p_e^2}{p_{\nu_e}^2}\frac{d\sigma_{e^-\,^2\mathrm{H}}}{d\Omega_{\nu_e} dp_{\nu_e}}(E_e^*)\right) \tilde{f}_{^2\mathrm{H}}(E_{^2\mathrm{H}})\, 2\, f_e(E_e)\,[1 - f_1(E_1)]\,[1 - f_2(E_2)]. \tag{C24}$$

Applying now detailed balance, $1/\lambda(E_{\nu_e}) = e^{\beta(E_{\nu_e} - \mu_{\nu_e}^{\mathrm{eq}})}\, j(E_{\nu_e})$ (for details, see Appendix C 5), and expressing the electron capture cross section by means of the neutrino-cross section, see Eq. (C23), computed in Ref. [76] one obtains the opacity,

$$\chi_{\nu_e\,nn}(E_{\nu_e}) = \frac{g_{^2\mathrm{H}}}{2}\int \frac{d^3p_{^2\mathrm{H}}}{(2\pi\hbar c)^3} d(\cos\theta) d\Omega_e dp_e \left(\frac{p_e^2}{p_{\nu_e}^2}\frac{d\sigma_{\bar{\nu}_e\,^2\mathrm{H}}}{d\Omega_e dp_{\nu_e}}(E_e^*)\right)[1 + \tilde{f}_{^2\mathrm{H}}(E_{^2\mathrm{H}})][1 - f_e(E_e)]\, f_1(E_1)\, 2\, f_2(E_2), \tag{C25}$$

with medium-modified electron energy as follows:

$$E_e^* = E_e + (m_{^2\mathrm{H}}^* - m_{^2\mathrm{H}}) - 2(m_n^* - m_n) + (U_d - 2U_n), \tag{C26}$$

and

$$p = \sqrt{m_n\left(E_e - E_{\nu_e} + m_{^2\mathrm{H}}^* - 2m_n^* + U_d - 2U_n\right)}, \tag{C27a}$$

$$E_1 = \frac{1}{2m_n^*}\left(\frac{p_{^2\mathrm{H}}^2}{4} + p^2 + pp_{^2\mathrm{H}}\cos\theta\right) + m_n^* + U_n, \quad E_2 = \frac{1}{2m_n^*}\left(\frac{p_{^2\mathrm{H}}^2}{4} + p^2 - pp_{^2\mathrm{H}}\cos\theta\right) + m_n^* + U_n. \tag{C27b}$$

Furthermore, we can integrate over the electron solid angle and recover the following expression:

$$\chi_{\nu\, N_1 N_2}(E_{\nu_e}) = \frac{g_{^2\mathrm{H}}}{4}\int \frac{d^3p_{^2\mathrm{H}}}{(2\pi\hbar c)^3} dp_e d(\cos\theta)\left(\frac{p_e^2}{p_{\nu_e}^2}\frac{d\sigma_{\bar{\nu}_e\,^2\mathrm{H}}}{dp_{\nu_e}}(E_e^*)\right)[1 + \tilde{f}_{^2\mathrm{H}}(E_{^2\mathrm{H}})][1 - f_e(E_e)]\, 2\, f_1(E_1)\, 2\, f_2(E_2). \tag{C28}$$

3. ν_e absorption on ^{3}H and $\bar{\nu}_e$ absorption on ^{3}He

For charged current ν_e-absorption on ^{3}H the situation is somewhat more complicated than for ^{2}H, because there are two components. The first one is the transition to the bound state of ^{3}He and the second component is the transition into the continuum with three final-state nucleons:

$$\nu_e + {}^3\mathrm{H} \to {}^3\mathrm{He} + e^-, \quad \nu_e + {}^3\mathrm{H} \to p + p + n + e^-, \tag{C29}$$

For the bound state to bound state reaction, we obtain the following opacity:

$$\chi_{\nu_e\,^3\mathrm{H}}(E_{\nu_e}) \simeq n_{^3\mathrm{H}}\, \sigma_{\nu_e\,^3\mathrm{H}}(E_{e^-})\,[1 - f_{e^-}(p_{e^-})], \tag{C30}$$

neglecting final-state ^{3}He blocking where we introduced the triton number density $n_{^3\mathrm{H}}$ and the corresponding cross section,

$$\sigma_{\nu_e\,^3\mathrm{H}}(E_{e^-}) = \frac{G^2}{\pi}\frac{1}{(\hbar c)^4}(p_{e^-}E_{e^-})\,\mathcal{B}_{\mathrm{GT}} \propto 2.26 \times 10^{-41}\left(\frac{E_{\nu_e}}{15\ \mathrm{MeV}}\right)\mathrm{cm}^2\mathrm{MeV}^{-2}, \tag{C31}$$

for a typical neutrino energy of 15 MeV, and with the Gammow-Teller transition amplitude, $\mathcal{B}_{\mathrm{GT}} = 5.87$, which is known from the triton decay. The following relation connects the medium modified electron energy relation:

$$E_{e^-} = E_{\nu_e} + (m_{^3\mathrm{H}} - m_{^3\mathrm{He}}) + (U_{^3\mathrm{H}} - U_{^3\mathrm{He}}), \tag{C32}$$

with the neutrino energy E_{ν_e} including the mass difference between ^{3}H and ^{3}He, $m_{^3\mathrm{H}} - m_{^3\mathrm{He}} = 0.5296$ (including electron

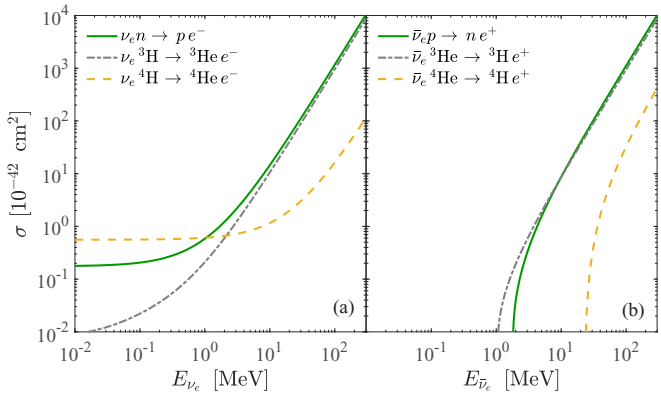

FIG. 13. Neutrino absorption cross section for reactions involving ^{3}H and ^{3}He (grey dash-dotted lines) as well as ^{4}H and ^{4}He (yellow dashed lines), in comparison to those for the charged current reactions (1)–(3) in Table I, for ν_e in graph (a) and $\bar{\nu}_e$ in graph (b).

contributions), and the mean-field potentials, $U_{^3\mathrm{H}}$ and $U_{^3\mathrm{He}}$. The latter quantities are provided by the gRDF(DD2) EOS.

From the comparison of the cross section of the charged current reactions (1)–(3) in Table I, for which $\sigma_{\nu_e N} \simeq 2.47 \times 10^{-41}$ cm^2 MeV^{-2}, again for a typical neutrino energy of 15 MeV, and with the transition standard amplitude, $g_V^2 + 3g_A^2$, with vector and axial-vector coupling constants, $g_V = 1.0$ and $g_A = 1.27$, it becomes evident that reactions involving ^{3}H and ^{3}He can become as important as the reactions involving the unbound nucleons, depending on the kinematics including final-state blocking contributions. This has already been realised in Ref. [2] at the level of the cross section analysis. Figure 13 compares these cross sections for ν_e (left panel) and $\bar{\nu}_e$ (right panel). We omit here the ^{3}H cross sections for the break-up reactions and the reactions involving ^{2}H (see therefore Ref. [2]).

The second component of the ν_e-absorption on triton in Eq. (C29) the transitions to the continuum, which is negligible compared to the bound state to bound state reaction as was shown in Ref. [2] based on the cross sections calculated in analogy to Ref. [13].

A similar expression as Eq. (C30) is obtained for the opacity of $\bar{\nu}_e$-absorption on ^{3}He,

$$\bar{\nu}_e + {}^3\mathrm{He} \to {}^3\mathrm{H} + e^+, \tag{C33}$$

as follows:

$$\chi_{\bar{\nu}_e\,{}^3\mathrm{He}}(E_{\bar{\nu}_e}) \simeq n_{^3\mathrm{He}}\, \sigma_{\bar{\nu}_e\,{}^3\mathrm{He}}(E_{\bar{\nu}_e})\,[1 - f_{e^+}(p_{e^+})]. \tag{C34}$$

The cross section, $\sigma_{\bar{\nu}_e\,{}^3\mathrm{He}}$, involves the same matrix element as Eq. (C31), and the following medium modified positron energy relation:

$$E_{e^+} = E_{\bar{\nu}_e} - (m_{^3\mathrm{H}} - m_{^3\mathrm{He}}) - (U_{^3\mathrm{H}} - U_{^3\mathrm{He}}), \tag{C35}$$

again with ^{3}H and ^{3}He masses and their mean-field potentials. Note that expression Eq. (C34) also neglects final state triton contributions. Also here the transition to the continuum, $\bar{\nu}_e\,{}^3\mathrm{H} \longrightarrow n\,n\,n\,e^+$, is negligible as was shown in Ref. [2], based on the cross section similar to those provided in Ref. [13].

TABLE IV. Thermally average cross section for Eq. (C36) comparing our fit Eqs. (C37)–(C38), with the cross sections provided in Ref. [79].

T [MeV]	$\langle\sigma\rangle_T$ [10^{-42} cm]	Ref. [79][a] [10^{-42} cm]
2	7.20(−5)	2.39(−5)
4	2.72(−2)	2.74(−2)
5	1.0(−1)	–
6	2.44(−1)	5.20(−1)
8	8.4(−1)	3.07

[a]Here we provide the total cross section.

4. $\bar{\nu}_e$ absorption on ^{4}He and ν_e absorption on ^{4}H

For the antineutrino charged current channel, there is the following bound state reaction:

$$\bar{\nu}_e + {}^4\mathrm{He} \to {}^4\mathrm{H} + e^+. \tag{C36}$$

The description of the final state ^{4}H is very challenge due to the presence of several broad resonances and the fact that the presence of a degenerate neutron background suppresses the emission of neutrons in the medium. Here, in a first attempt to take this process into account, we use the thermally-averaged inclusive cross sections, $\langle\sigma\rangle_T$, that have been provided in Ref. [79], assuming a thermal neutrino distribution with zero chemical potential, and assume that in the medium all neutron emission channels are suppressed. To be able to implement them into the collision integral of `AGILE-BOLTZTRAN`, we reverse engineer in order to obtain the transition amplitude as follows:

$$\langle\sigma\rangle_T = \frac{4\pi}{(hc)^3}\frac{1}{n_\nu}\int dE_{\bar{\nu}_e} E_{\bar{\nu}_e}^2\, \sigma_{\bar{\nu}_e\,{}^4\mathrm{He}}(E_{e^+})\, f_{\bar{\nu}_e}^{\mu_{\bar{\nu}_e}=0}(E_{\bar{\nu}_e}; T), \tag{C37}$$

with neutrino number density, n_ν, and we set

$$\sigma_{\bar{\nu}_e\,{}^4\mathrm{He}}(E_{e^+}) = \frac{G^2}{\pi}\frac{1}{(\hbar c)^4}(p_{e^+}E_{e^+})\,\mathcal{B}_{\mathrm{GT}}, \tag{C38}$$

assuming a constant value of $\mathcal{B}_{\mathrm{GT}} = 0.34$. This approximation is fitted to reproduce the cross section per nucleon in Ref. [79] in the temperature range of $T \simeq 5$–10 MeV (see Table IV) within a factor of 2 or less. However, it certainly overestimates the thermally averaged cross sections at low temperatures by about an order of magnitude. Similarly as before, the antineutrino and positron energies are related via the restmass and mean-field potential differences of ^{4}H and ^{4}He as follows:

$$E_{e^+} = E_{\bar{\nu}_e} - (m_{^4\mathrm{H}} - m_{^4\mathrm{He}}) - (U_{^4\mathrm{H}} - U_{^4\mathrm{He}}). \tag{C39}$$

Then, the opacity for Eq. (C36) in the elastic approximation reads as follows:

$$\chi_{\bar{\nu}_e\,{}^4\mathrm{He}}(E_{\bar{\nu}_e}) = n_{^4\mathrm{He}}\, \sigma_{\bar{\nu}_e\,{}^4\mathrm{He}}(E_{e^+})[1 - f_{e^+}(E_{e^+})], \tag{C40}$$

with the ^{4}He number density denoted as $n_{^4\mathrm{He}}$.

The matrix element entering in the cross section above for neutrino absorption on ^{4}H,

$$\nu_e + {}^4\mathrm{H} \longrightarrow {}^4\mathrm{He} + e^-, \tag{C41}$$

is generally not known for this reaction in vacuum and furthermore should be modified due to the in-medium effects. However, assuming mirror symmetry between ^{4}H and ^{4}Li, it is taken to be a factor of 5 smaller than the one for Eq. (C36), which yields $\mathcal{B}_{\rm GT} = 0.068$. Note that here we consider only transitions to bound states in ^{4}He as they are energetically favored. Similarly as for the processes involving ^{3}H and ^{3}He in Sec. C 3, we express the reaction rate for Eq. (C41) as follows:

$$\chi_{\nu_e\,^4\mathrm{H}}(E_{\nu_e}) = n_{^4\mathrm{H}}\,\sigma_{\nu_e\,^4\mathrm{H}}(E_{e^-})\,[1 - f_{e^-}(E_{e^-})], \tag{C42}$$

with ^{4}H number density, $n_{^4\mathrm{H}}$, and the following medium modified relation between electron and neutrino energies,

$$E_{e^-} = E_{\nu_e} + (m_{^4\mathrm{H}} - m_{^4\mathrm{He}}) + (U_{^4\mathrm{H}} - U_{^4\mathrm{He}}). \tag{C43}$$

The cross section,

$$\sigma_{\nu_e\,^4\mathrm{H}}(E_{e^-}) = \frac{G^2}{\pi}\frac{1}{(\hbar c)^4}(p_{e^-}E_{e^-})\,\mathcal{B}_{\rm GT}, \tag{C44}$$

is also shown in Fig. 13 in the left panel (yellow dashed line).

5. Detailed balance

Here we will derive the detailed balance relation for the (anti)neutrino emissivity $j(E_\nu)$, i.e., the reverse reactions,

$$e^- + p + p \longrightarrow {}^2\mathrm{H} + \nu_e, \quad e^+ + n + n \longrightarrow {}^2\mathrm{H} + \bar{\nu}_e,$$

for which the reaction rate is given by the following expression,

$$j_{\nu_e\,^2\mathrm{H}}(E_\nu) = \frac{2\pi G^2}{\hbar c}\frac{1}{(2\pi\hbar c)^3}\int\frac{d^3p_{^2\mathrm{H}}}{(2\pi\hbar c)^3}\frac{d^3p_e}{(2\pi\hbar c)^3}2\pi p^2\,d(\cos\theta)\,|M|^2\left\{1+\tilde{f}_{^2\mathrm{H}}(E_{^2\mathrm{H}})\right\}f_e(E_e)\,f_1(E_1)\,f_2(E_2). \tag{C45}$$

Comparing this expression with Eq. (C10) one obtains,

$$\begin{aligned} j_{\nu_e\,^2\mathrm{H}}(E_\nu) &= \frac{2\pi G^2}{\hbar c}\frac{1}{(2\pi\hbar c)^3}\int\frac{d^3p_{^2\mathrm{H}}}{(2\pi\hbar c)^3}\frac{d^3p_e}{(2\pi\hbar c)^3}2\pi p^2\,d(\cos\theta)\,|M|^2\exp\{\beta(E_{^2\mathrm{H}}-\mu_{^2\mathrm{H}})\}\tilde{f}_{^2\mathrm{H}}(E_{^2\mathrm{H}}) \\ &\quad\times\exp\{-\beta(E_e-\mu_e)\}(1-f_e(E_e))\exp\{-\beta(E_1-\mu_1)\}[1-f_1(E_1)]\exp\{-\beta(E_2-\mu_2)\}[1-f_2(E_2)] \qquad \text{(C46)} \\ &= \frac{2\pi G^2}{\hbar c}\frac{1}{(2\pi\hbar c)^3}\int\frac{d^3p_{^2\mathrm{H}}}{(2\pi\hbar c)^3}\frac{d^3p_e}{(2\pi\hbar c)^3}2\pi p^2\,d(\cos\theta)\,|M|^2 \\ &\quad\times\exp\left\{-\beta\left(E_{\nu_e}-\mu_{\nu_e}^{\rm eq}\right)\right\}\tilde{f}_{^2\mathrm{H}}(E_{^2\mathrm{H}})[1-f_e(E_e)][1-f_1(E_1)][1-f_2(E_2)] \\ &= \exp\left\{-\beta\left(E_{\nu_e}-\mu_{\nu_e}^{\rm eq}\right)\right\}\chi_{\nu_e\,^2\mathrm{H}}(E_{\nu_e}), \qquad \text{(C47)} \end{aligned}$$

with the neutrino equilibrium chemical potential, $\mu_{\nu_e}^{\rm eq} = \mu_e + \mu_p + \mu_p - \mu_{^2\mathrm{H}} = \mu_e - (\mu_n - \mu_p)$. Note that this is the same detailed balance relation as for the charged current absorption processes with free nucleons (reactions (1) and (2) in Table I). Applying the same approach for the reverse triton opacity, i.e., the emissivities for the following processes:

$$\begin{aligned} e^-\,{}^2\mathrm{H} &\longrightarrow p\,p\,\nu_e, \quad & e^+\,{}^2\mathrm{H} &\longrightarrow n\,n\,\bar{\nu}_e, \\ e^-\,{}^3\mathrm{He} &\longrightarrow {}^3\mathrm{H}\,\nu_e, \quad & e^+\,{}^3\mathrm{H} &\longrightarrow {}^3\mathrm{He}\,\bar{\nu}_e, \\ e^-\,{}^4\mathrm{He} &\longrightarrow {}^4\mathrm{H}\,\nu_e, \quad & e^+\,{}^4\mathrm{H} &\longrightarrow {}^4\mathrm{He}\,\bar{\nu}_e, \end{aligned}$$

one will recover the same detailed balance relation Eq. (C47).

[1] H.-T. Janka, K. Langanke, A. Marek, G. Martínez-Pinedo, and B. Müller, Phys. Rep. **442**, 38 (2007).
[2] T. Fischer, N.-U. Bastian, D. Blaschke, M. Cierniak, M. Hempel, T. Klähn, G. Martínez-Pinedo, W. G. Newton, G. Röpke, and S. Typel, Publ. Astron. Soc. Austr. **34**, e067 (2017).
[3] H.-T. Janka, Ann. Rev. Nucl. Part. Sci. **62**, 407 (2012).
[4] B. Müller, Publ. Astron. Soc. Austr. **33**, e048 (2016).
[5] B. Schuetrumpf, G. Martínez-Pinedo, M. Afibuzzaman, and H. M. Aktulga, Phys. Rev. C **100**, 045806 (2019).
[6] J. M. Lattimer and F. Swesty, Nucl. Phys. A **535**, 331 (1991).
[7] A. S. Schneider, L. F. Roberts, and C. D. Ott, Phys. Rev. C **96**, 065802 (2017).
[8] H. Shen, H. Toki, K. Oyamatsu, and K. Sumiyoshi, Prog. Theor. Phys. **100**, 1013 (1998).
[9] M. Hempel and J. Schaffner-Bielich, Nucl. Phys. A **837**, 210 (2010).
[10] S. Furusawa, S. Yamada, K. Sumiyoshi, and H. Suzuki, Astrophys. J. **738**, 178 (2011).
[11] S. Furusawa, H. Nagakura, K. Sumiyoshi, and S. Yamada, Astrophys. J. **774**, 78 (2013).
[12] K. Sumiyoshi and G. Röpke, Phys. Rev. C **77**, 055804 (2008).
[13] A. Arcones, G. Martínez-Pinedo, E. O'Connor, A. Schwenk, H.-T. Janka, C. J. Horowitz, and K. Langanke, Phys. Rev. C **78**, 015806 (2008).
[14] A. V. Yudin, M. Hempel, S. I. Blinnikov, D. K. Nadyozhin, and I. V. Panov, Mon. Not. Roy. Astron. Soc. **483**, 5426 (2019).
[15] L. Qin, K. Hagel, R. Wada, J. B. Natowitz, S. Shlomo, A. Bonasera, G. Röpke, S. Typel, Z. Chen, M. Huang, J. Wang, H. Zheng, S. Kowalski, M. Barbui, M. R. D. Rodrigues, K. Schmidt, D. Fabris, M. Lunardon, S. Moretto, G. Nebbia, S. Pesente, V. Rizzi, G. Viesti, M. Cinausero, G. Prete, T. Keutgen, Y. El Masri, Z. Majka, and Y. G. Ma, Phys. Rev. Lett. **108**, 172701 (2012).

[16] H. Pais, R. Bougault, F. Gulminelli, C. Providência, E. Bonnet, B. Borderie, A. Chbihi, J. D. Frankland, E. Galichet, D. Gruyer, M. Henri, N. Le Neindre, O. Lopez, L. Manduci, M. Parlôg, and G. Verde, Phys. Rev. Lett. **125**, 012701 (2020).

[17] G. Röpke, Phys. Rev. C **101**, 064310 (2020).

[18] M. Hempel, K. Hagel, J. Natowitz, G. Röpke, and S. Typel, Phys. Rev. C **91**, 045805 (2015).

[19] S. Typel, G. Röpke, T. Klähn, D. Blaschke, and H. H. Wolter, Phys. Rev. C **81**, 015803 (2010).

[20] H. Pais, F. Gulminelli, C. Providência, and G. Röpke, Phys. Rev. C **97**, 045805 (2018).

[21] H. Pais, F. Gulminelli, C. Providência, and G. Röpke, Phys. Rev. C **99**, 055806 (2019).

[22] G. Röpke, Phys. Rev. C **79**, 014002 (2009).

[23] G. Röpke, Nucl. Phys. A **867**, 66 (2011).

[24] H. Pais and S. Typel, *Nuclear Particle Correlations and Cluster Physics*, edited by Wolf-Udo Schröder (World Scientific, Singapore, 2016).

[25] EOS tables are available at the comPOSE data page under https://compose.obspm.fr.

[26] M. Oertel, M. Hempel, T. Klähn, and S. Typel, Rev. Mod. Phys. **89**, 015007 (2017).

[27] K. Langanke and G. Martínez-Pinedo, Rev. Mod. Phys. **75**, 819 (2003).

[28] K. Langanke, G. Martinez-Pinedo, B. Müller, H.-T. Janka, A. Marek, W. R. Hix, A. Juodagalvis, and J. M. Sampaio, Phys. Rev. Lett. **100**, 011101 (2008).

[29] G. M. Fuller and B. S. Meyer, Astrophys. J. **376**, 701 (1991).

[30] T. Fischer, K. Langanke, and G. Martínez-Pinedo, Phys. Rev. C **88**, 065804 (2013).

[31] T. Fischer, G. Guo, A. A. Dzhioev, G. Martínez-Pinedo, M.-R. Wu, A. Lohs, and Y.-Z. Qian, Phys. Rev. C **101**, 025804 (2020).

[32] A. Juodagalvis, K. Langanke, W. R. Hix, G. Martínez-Pinedo, and J. M. Sampaio, Nucl. Phys. A **848**, 454 (2010).

[33] A. Mezzacappa and S. W. Bruenn, Astrophys. J. **405**, 637 (1993).

[34] C. J. Horowitz, Phys. Rev. D **65**, 043001 (2002).

[35] A. Mezzacappa and S. W. Bruenn, Astrophys. J. **410**, 740 (1993).

[36] S. W. Bruenn, Astrophys. J. Suppl. **58**, 771 (1985).

[37] S. Hannestad and G. Raffelt, Astrophys. J. **507**, 339 (1998).

[38] T. Fischer, Astron. Astrophys. **593**, A103 (2016).

[39] R. Buras, M. Rampp, H.-T. Janka, and K. Kifonidis, Astron. Astrophys. **447**, 1049 (2006).

[40] T. Fischer, S. C. Whitehouse, A. Mezzacappa, F.-K. Thielemann, and M. Liebendörfer, Astron. Astrophys. **499**, 1 (2009).

[41] A. Mezzacappa and S. W. Bruenn, Astrophys. J. **405**, 669 (1993).

[42] M. Liebendörfer, O. E. B. Messer, A. Mezzacappa, S. W. Bruenn, C. Y. Cardall, and F.-K. Thielemann, Astrophys. J. Suppl. **150**, 263 (2004).

[43] M. Liebendörfer, S. Rosswog, and F.-K. Thielemann, Astrophys. J. Suppl. **141**, 229 (2002).

[44] M. Liebendörfer, M. Rampp, H.-T. Janka, and A. Mezzacappa, Astrophys. J. **620**, 840 (2005).

[45] E. O'Connor, R. Bollig, A. Burrows, S. Couch, T. Fischer, H.-T. Janka, K. Kotake, E. J. Lentz, M. Liebendörfer, O. E. B. Messer, A. Mezzacappa, T. Takiwaki, and D. Vartanyan, J. Phys. G Nucl. Phys. **45**, 104001 (2018).

[46] H. Shen, H. Toki, K. Oyamatsu, and K. Sumiyoshi, Nucl. Phys. A **637**, 435 (1998).

[47] M. Hempel, T. Fischer, J. Schaffner-Bielich, and M. Liebendörfer, Astrophys. J. **748**, 70 (2012).

[48] A. W. Steiner, M. Hempel, and T. Fischer, Astrophys. J. **774**, 17 (2013).

[49] F. X. Timmes and D. Arnett, Astrophys. J. Suppl. **125**, 277 (1999).

[50] S. Reddy, M. Prakash, and J. M. Lattimer, Phys. Rev. D **58**, 013009 (1998).

[51] G. Martínez-Pinedo, T. Fischer, A. Lohs, and L. Huther, Phys. Rev. Lett. **109**, 251104 (2012).

[52] L. F. Roberts, S. Reddy, and G. Shen, Phys. Rev. C **86**, 065803 (2012).

[53] M. Hempel, Phys. Rev. C **91**, 055807 (2015).

[54] T. Fischer, M. Hempel, I. Sagert, Y. Suwa, and J. Schaffner-Bielich, Eur. Phys. J. A **50**, 46 (2014).

[55] M. Wang, G. Audi, F. G. Kondev, W. Huang, S. Naimi, and X. Xu, Chin. Phys. C **41**, 030003 (2017).

[56] J. Duflo and A. P. Zuker, Phys. Rev. C **52**, 23 (1995).

[57] G. Röpke, *Nuclear Particle Correlations and Cluster Physics*, edited by Wolf-Udo Schröder (World Scientific, Singapore, 2017).

[58] S. Typel, J. Phys. G **45**, 114001 (2018).

[59] S. Typel and H. Pais, Nuovo Cim. C **39**, 393 (2017).

[60] M. Schmidt, G. Röpke, and H. Schulz, Ann. Phys. **202**, 57 (1990).

[61] C. J. Horowitz and A. Schwenk, Nucl. Phys. A **776**, 55 (2006).

[62] G. Shen, C. J. Horowitz, and E. O'Connor, Phys. Rev. C **83**, 065808 (2011).

[63] M. D. Voskresenskaya and S. Typel, Nucl. Phys. A **887**, 42 (2012).

[64] G. Röpke, N.-U. Bastian, D. Blaschke, T. Klähn, S. Typel, and H. H. Wolter, Nucl. Phys. A **897**, 70 (2013).

[65] I. Tews, T. Krüger, K. Hebeler, and A. Schwenk, Phys. Rev. Lett. **110**, 032504 (2013).

[66] T. Krüger, I. Tews, K. Hebeler, and A. Schwenk, Phys. Rev. C **88**, 025802 (2013).

[67] B. P. Abbott, LIGO Scientific Collaboration, and Virgo Collaboration, Phys. Rev. Lett. **121**, 161101 (2018).

[68] S. De, D. Finstad, J. M. Lattimer, D. A. Brown, E. Berger, and C. M. Biwer, Phys. Rev. Lett. **121**, 091102 (2018).

[69] B. P. Abbott, LIGO Scientific Collaboration, and Virgo Collaboration, Astrophys. J. **892**, L3 (2020).

[70] M. C. Miller, F. K. Lamb, A. J. Dittmann, S. Bogdanov, Z. Arzoumanian, K. C. Gendreau, S. Guillot, A. K. Harding, W. C. G. Ho, J. M. Lattimer, R. M. Ludlam, S. Mahmoodifar, S. M. Morsink, P. S. Ray, T. E. Strohmayer, K. S. Wood, T. Enoto, R. Foster, T. Okajima, G. Prigozhin, and Y. Soong, Astrophys. J. **887**, L24 (2019).

[71] J. Antoniadis, P. C. C. Freire, N. Wex, T. M. Tauris, R. S. Lynch, M. H. van Kerkwijk, M. Kramer, C. Bassa, V. S. Dhillon, T. Driebe, J. W. T. Hessels, V. M. Kaspi, V. I. Kondratiev, N. Langer, T. R. Marsh, M. A. McLaughlin, T. T. Pennucci, S. M. Ransom, I. H. Stairs, J. van Leeuwen, J. P. W. Verbiest, and D. G. Whelan, Science **340**, 448 (2013).

[72] H. T. Cromartie, E. Fonseca, S. M. Ransom, P. B. Demorest, Z. Arzoumanian, H. Blumer, P. R. Brook, M. E. DeCesar, T. Dolch, J. A. Ellis, R. D. Ferdman, E. C. Ferrara, N. Garver-Daniels, P. A. Gentile, M. L. Jones, M. T. Lam, D. R. Lorimer, R. S. Lynch, M. A. McLaughlin, C. Ng, D. J. Nice, T. T.

Pennucci, R. Spiewak, I. H. Stairs, K. Stovall, J. K. Swiggum, and W. W. Zhu, Nat. Astron. **4**, 72 (2020).
[73] S. Woosley, A. Heger, and T. Weaver, Rev. Mod. Phys. **74**, 1015 (2002).
[74] T. Fischer, Eur. Phys. J. A **52**, 54 (2016).
[75] K. Sumiyoshi, C. Ishizuka, A. Ohnishi, S. Yamada, and H. Suzuki, Astrophys. J. **690**, L43 (2009).
[76] S. Nakamura, T. Sato, V. Gudkov, and K. Kubodera, Phys. Rev. C **63**, 034617 (2001).
[77] T. Fischer, G. Martínez-Pinedo, M. Hempel, L. Huther, G. Röpke, S. Typel, and A. Lohs, Eur. Phys. J. Web Conf. **109**, 06002 (2016).
[78] G. Shen, L. E. Marcucci, J. Carlson, S. Gandolfi, and R. Schiavilla, Phys. Rev. C **86**, 035503 (2012).
[79] D. Gazit and N. Barnea, Phys. Rev. Lett. **98**, 192501 (2007).
[80] T. Fischer, G. Martínez-Pinedo, M. Hempel, and M. Liebendörfer, Phys. Rev. D **85**, 083003 (2012).
[81] G. Martínez-Pinedo, T. Fischer, and L. Huther, J. Phys. G Nucl. Phys. **41**, 044008 (2014).
[82] E. O'Connor, D. Gazit, C. J. Horowitz, A. Schwenk, and N. Barnea, Phys. Rev. C **75**, 055803 (2007).
[83] M. Hempel, J. Schaffner-Bielich, S. Typel, and G. Röpke, Phys. Rev. C **84**, 055804 (2011).
[84] S. Furusawa, K. Sumiyoshi, S. Yamada, and H. Suzuki, Astrophys. J. **772**, 95 (2013).
[85] Y. Suwa, T. Takiwaki, K. Kotake, T. Fischer, M. Liebendörfer, and K. Sato, Astrophys. J. **764**, 99 (2013).
[86] A. Marek, H.-T. Janka, and B. Müller, Astron. Astrophys. **496**, 475 (2009).
[87] T. Melson, H.-T. Janka, R. Bollig, F. Hanke, A. Marek, and B. Müller, Astrophys. J. **808**, L42 (2015).
[88] R. Bollig, H.-T. Janka, A. Lohs, G. Martínez-Pinedo, C. J. Horowitz, and T. Melson, Phys. Rev. Lett. **119**, 242702 (2017).
[89] H. Yasin, S. Schäfer, A. Arcones, and A. Schwenk, Phys. Rev. Lett. **124**, 092701 (2020).